MICROSTUCTURAL ENGINEERING OF Mn ALLOYED AUSTENITIC STEEL FOR HYDROGEN STORAGE AND DELIVERY

by

Pawan Kathayat

A thesis submitted to the Faculty and the Board of Trustees of the Colorado School of Mines in partial fulfillment of the requirements for the degree of Master of Science (Metallurgical and Materials Engineering).

Golden, Colorado

Date: _____

Signed: _____

Pawan Kathayat

Signed: _____

Dr. Kip O. Findley

Thesis Advisor

Signed: _____

Dr. Lawrence Cho

Thesis Advisor

Signed: _____

Dr. John Speer

Committee Member

Signed: _____

Dr. Emmanuel De Moor

Committee Member

Signed: _____

Dr. Ivar Reimanis

Department Head

Department of Metallurgical and Materials Engineering

ABSTRACT

Hydrogen is a potential fuel source for automotive and heavy equipment applications, with the only byproduct being water; it has also been used as an alternative to coal for the carbon-free, sustainable manufacturing of "green" iron and steel. One challenging task for implementing hydrogen technology is the infrastructure cost. The alloys widely used for hydrogen fueling infrastructure are austenitic stainless steels because of their high resistance against hydrogen embrittlement. These alloys have a high nickel (Ni) content, the cost of which is relatively high. It is, therefore, essential to develop lower-cost options without significantly lowering the hydrogen embrittlement resistance and mechanical properties. In this study, high manganese (Mn) austenitic alloys were designed as an alternative to high Ni austenitic stainless steel alloys because the cost of Mn is substantially lower than Ni. In addition, Mn, similar to Ni, is a powerful austenite stabilizer. Two heats of high Mn alloys with different stacking fault energies (SFE) of ~29 $mJ \cdot m^{-2}$ and 49 $mJ \cdot m^{-2}$ were acquired, and on the basis of their hydrogen performance, a new vanadium (V)-microalloyed high Mn alloy was designed. The V-microalloyed high Mn alloy composition was designed to achieve a stacking fault energy above 39 $mJ \cdot m^{-2}$ to avoid planar slip deformation mechanisms, including deformation-induced twinning and ε-martensite formation. V was added to the designed alloy for thermomechanical processing and potential precipitate strengthening. Post-processing parameters such as cold working and cold working in conjunction with aging were performed with the V-microalloyed high Mn steel. Hydrogen embrittlement characteristics of the designed high Mn steels having different SFE values were compared against 316L stainless steel, which was received in a cold-rolled condition. Hydrogen embrittlement sensitivity was investigated using circular notch tensile specimens cathodically charged with hydrogen in a 0.05M NaOH electrolytic solution.

The 316L stainless steel exhibited no notch strength loss, and the fracture surfaces showed ductile fracture features regardless of the testing environment, which validated its high hydrogen embrittlement resistance. The high Mn alloys with SFE of ~29 $mJ \cdot m^{-2}$ and 49 $mJ \cdot m^{-2}$ had notch strength losses of 11 pct and 6 pct, respectively. When tested in hydrogen, the high Mn steel with low SFE exhibited transgranular (brittle) fracture, whereas the high Mn steel with high SFE exhibited only ductile fracture, similar to the 316L stainless steel. The ε-martensite phase was detected in the high Mn steel with SFE of ~29 $mJ \cdot m^{-2}$ condition after tensile deformation, which is consistent with its lower SFE. The V-microalloyed high Mn steel in the as-hot-rolled condition had a notch strength loss of 17 pct, and demonstrated intergranular (brittle) fracture with some ductile fracture features, i.e. dimples, observed near the notch root of the fractured specimen. The V-microalloyed high Mn steel in the cold worked condition had notch strength loss of 5 pct, and showed brittle fracture. The V-microalloyed high Mn steel in the cold worked and aged condition indicated no notch strength loss in hydrogen, and the fracture surface showed ductile features at the root notch, indicating comparable performance to 316L stainless steel.

TABLE OF CONTENTS

LIST OF FIGURES

LIST OF TABLES

ACKNOWLEDGEMENTS

I want to thank the US Department of Energy H2@Scale for supporting this project.

I want to thank my advisors, Dr. Kip Findley, and Dr. Lawrence Cho, for their mentorship and guidance throughout this project. I grew as a person both in a professional and personal capacity.

I would like to thank my committee, Dr. John Speer, and Dr. Emmanuel De Moor, for their technical advice.

Thanks to my industrial mentors N. Pottore from ArcelorMittal and K. Zeik from US Steel, for the project feedback. Special thanks to ASPPRC for providing the environment where I could get technical feedback from industry professionals. I want to acknowledge people associated with ASPPRC for helping me in multiple ways throughout my master's journey.

I want to thank my colleague Jason for helping me. I would also like to thank my office mates for their moral support.

Finally, I want to thank my parents, Tribhuwan and Geeta, and my sister Priyanka. Thank you to all the friends I have made in Colorado.

CHAPTER 1: INTRODUCTION

1.1. Project Motivation

Hydrogen is a potential fuel source for automotive and heavy equipment applications, with the only by-product being water; it has also been used as an alternative to coal for the carbon-free, sustainable manufacturing of "green" iron and steel. One challenge for implementing this technology is the infrastructure cost. Austenitic stainless steels are commonly used for hydrogen infrastructure, which includes compressors, storage tanks, valves, etc. They have high resistance against hydrogen embrittlement. These alloys have high Ni content, the cost of which is relatively high. It is crucial to develop low-cost alloys without significantly lowering the hydrogen embrittlement resistance and mechanical properties. In this study, high Mn austenitic alloys are designed as an alternative considering the substantially lower cost of Mn compared to Ni. In addition, Mn, similar to Ni, is a powerful austenite stabilizer

The austenite phase stability and stacking fault energy (SFE) play an influential role in hydrogen embrittlement resistance. SFE influences the deformation mechanisms; planar slip mechanisms such as deformation induced twinning and martensite formation promote hydrogen embrittlement for austenitic alloys. Thermodynamic SFE models can be utilized to design alloy compositions with relatively high SFE and a deformation mechanism that promotes high resistance against hydrogen embrittlement. Gibbs *et al*. [53] developed a thermodynamic model to predict SFE and proposed a threshold SFE value (39 $mJ \cdot m^{-2}$) above which the 300 series austenitic stainless steels and Mn stabilized stainless steels have a better hydrogen embrittlement resistance.

The alloys investigated in this study were 316L stainless steel, high Mn austenitic alloys, and a designed V-microalloyed high Mn austenitic steel. These alloys are compared with respect to microstructure, mechanical properties, hydrogen embrittlement resistance, and deformation mechanism. The alloy composition of the designed V-microalloyed high Mn steel is selected based on thermodynamic modeling of SFE, literature review, and a preliminary study of different grades of high Mn austenitic alloys. V is added to the designed steel for grain refinement and precipitation hardening during aging. Post-processing including cold working and aging was performed on the designed V-microalloyed high Mn steel to investigate its effect on strength and hydrogen embrittlement susceptibility of the steel.

Research Questions:

This project aims to develop low-cost austenitic high Mn steels with high hydrogen embrittlement resistance. Two research questions have been developed:

- Does SFE, calculated based on thermodynamic modeling, predict hydrogen embrittlement resistance for high Mn alloys?
- How do post-processing parameters like cold working and aging affect the hydrogen performance of the designed V-microlloyed high Mn steel?

1.2. Thesis Overview

Chapter 2 contains the background and literature review of hydrogen embrittlement in austenitic alloys. A comparison of high Ni with high Mn alloys regarding hydrogen performance is presented. The relationship between SFE, deformation mechanisms, and hydrogen performance of austenitic alloys is analyzed. The thermodynamic modeling of SFE applied in this project is introduced. Gaseous hydrogen charging is compared against cathodic charging with different electrolytic solutions. The strengthening mechanisms of the austenitic alloys are discussed. The post-processing routes of high Mn austenitic alloys are analyzed.

Chapter 3 consists of the experimental methodologies, which include mechanical tests in different environments and characterization of the austenitic alloys, and processing for the designed V-microalloyed high Mn steel.

The results and discussion are presented in Chapter 4, incorporating microstructural analysis, mechanical properties, hydrogen embrittlement test results, and fractographic analysis of austenitic alloys investigated in this thesis. The effect of the post-processing parameters like cold working and aging of the designed V-microalloyed high Mn steel, and their impact on hydrogen embrittlement are also examined in Chapter 4.

The summary and conclusions of this research project are presented in Chapter 5.

CHAPTER 2: BACKGROUND

2.1. Hydrogen Embrittlement in Austenitic Alloys

Austenitic stainless steels such as 301-, 304-, and 316-type steels are conventional alloys used for manufacturing storage containers, pipes, valves, and containers used for hydrogen environments as they satisfy the requirements for strength, toughness, and hydrogen embrittlement resistance. Understanding the mechanisms of hydrogen embrittlement, the concept of hydrogen traps, and the influence of hydrogen on fracture are integral in understanding hydrogen embrittlement in austenitic alloys. These items are discussed in the sub-sections given below.

2.1.1. Mechanisms of Hydrogen Embrittlement

There is no consensus among the scientific community regarding hydrogen embrittlement mechanisms. The principal mechanisms which are generally accepted are given below.

a) Hydrogen enhanced decohesion (HEDE)

It is theorized that when hydrogen is absorbed by the metal, there is a reduction of interatomic bond energy which increases decohesion. Trapping sites like grain boundaries contain hydrogen, which reduces the cohesive strength locally and contributes to hydrogen embrittlement [1]. Zaferani *et al.* [3] state that hydrogen embrittlement occurs in the fracture process zone (FPZ) when the local crack tip opening tensile stress exceeds the maximum-local atomic cohesion strength, which is lowered by the presence of hydrogen. Wang *et al*. [4] used computer simulation techniques based on the works of Daw *et al.* [5], Solanki *et al.* [6] and Plimpton *et al.* [7] to calculate the change in the bond strength due to hydrogen in α-Fe. Figure 2.1 shows the influence of hydrogen gas pressure on the grain boundary cohesive energy (Σ5(120)) in Fe; as the hydrogen pressure increases, the cohesive energy decreases.

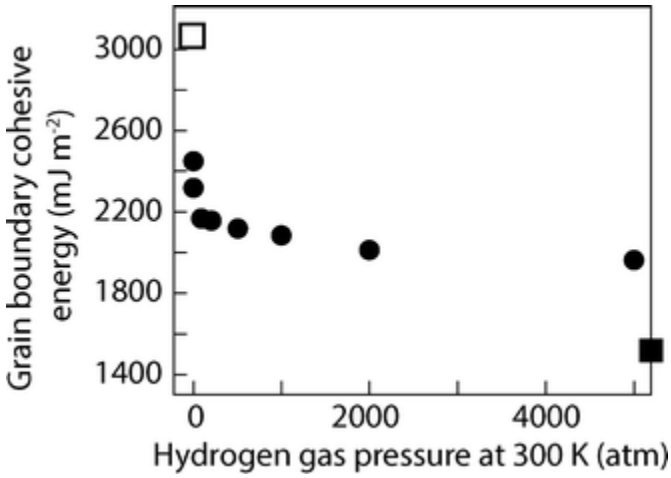

Figure 2.1: Grain boundary cohesive energy as a function of hydrogen gas pressure for a ∑5(120) grain boundary in Fe. Open square—no hydrogen; filled square—gas pressure is 48,346 atm (5 GPa) (highest gas pressure) [8].

b) Hydrogen enhanced local plasticity (HELP)

Researchers have theorized this mechanism since the 1970s [9-11]. The HELP mechanism states that hydrogen interacts with dislocations (similar to the Cottrell environment) and increases their mobility, leading to crack propagation and fracture. Fractures are brittle in nature. Ferreira *et al.* [12] performed in situ deformation testing with 310 stainless steel in a transmission electron microscope (TEM) with electron transparent foils with thicknesses of less than 200 nm in air and hydrogen gas. It was observed that the dislocation mobility increased in the presence of hydrogen gas, leading to an increase in dislocation density at interfaces such as grain boundaries. It should be pointed out that in situ TEM was performed in thin films without any plastic constraint, which might not simulate actual service conditions [2].

c) Hydrogen-induced phase transformation

This mechanism has been experimentally observed in austenitic stainless steels and Fe-Mn alloys [13-14]. Hydrogen affects the austenitic phase stability, possibly promoting the transformation of the γ austenite phase (FCC) into strain-induced ε- martensite (HCP) and α-martensite (BCC). Austenitic alloys (like 310 series stainless steels) did not exhibit brittle fracture (hydrogen embrittlement) in hydrogen-charged conditions due to their austenitic phase stability [14]. However, strain-induced martensite leads to brittle fracture in austenitic alloys like 304 SS [14]. Figure 2.2 shows peak engineering stress versus fracture strain data for 304L, 316L and 10-8-2.5, all austenitic alloys. In the hydrogen environment, 304L had poor strength and elongation parameters compared to 316L and 10-8-2.5, which the authors attributed to lower

austenite stability in the 304L alloy [15]. The correlation between austenite stability and hydrogen embrittlement will be discussed in Chapter 4.

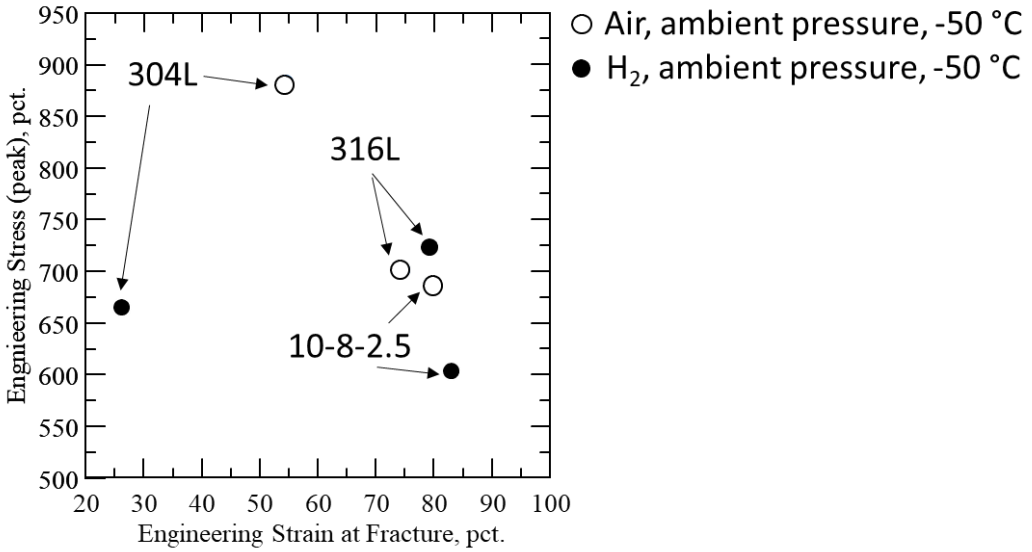

Figure 2.2: Engineering stress (peak) versus strain at fracture of alloys 304L, 316L, and 10-8-2.5 obtained at −50 °C in air (atmospheric pressure) and 40 MPa hydrogen gas [15].

2.1.2. Hydrogen Trapping and Permeation

Hydrogen trapping has been argued to reduce hydrogen mobility and thus mitigate associated embrittlement. Bhadeshia [16] states that diffusible hydrogen causes damage, as it interacts with stress concentrations such as tips of sharp cracks; this process accelerates fracture based on Darken *et al*.'s findings [17]. Hydrogen interacts with traps like dislocations and impedes hydrogen diffusion in the steel. Hydrogen traps can be classified into two types, namely reversible and irreversible traps. The energy associated with trapped hydrogen is called the binding energy (E_b). Maroef *et al.* [18] stated that the traps with a binding energy of more than 60 kJ mol^{-1} can be classified as irreversible based on hydrogen permeation measurements using electrochemical charging carried out isothermally at room temperature. Irreversible traps with a binding energy of 100 kJ mol^{-1} at ambient temperature might become reversible at elevated temperatures [16]. It is postulated that strong traps (irreversible) reduce the susceptibility to hydrogen embrittlement [16,18-19].

There are two methodologies of deriving hydrogen trap energy. First, hydrogen permeation experiments directly yield E_b. Secondly, thermal desorption experiments give the

summation of E_b+Q, where Q is the activation energy for detrapping [16-18]. In hydrogen permeation testing, it is assumed that the irreversible traps would continuously absorb hydrogen until saturation, which might lead to a time lag in permeation through the specimen. Different heating rates are applied in hydrogen desorption testing to obtain trapping energies. The McNabb and Foster model [20] is widely used in computing E_b, and Q. Both permeation and hydrogen desorption parameters can be fitted into the following equation:

$$\frac{d\theta_t}{dt} = kC_1(1-\theta_t) - p\theta_t \; where \; \theta_t = \frac{C_t}{N_t} \tag{2.1}$$

Here, θ_t is the occupancy of trap sites by hydrogen atoms, N_t is the density of the traps. C_1 and C_t are the hydrogen concentrations in lattice and trap sites, respectively. *k* and *p* are rates of trapping and escaping, respectively. The rate of hydrogen trapping and escaping can be calculated using the following equations:

$$k = k_0 \exp\left\{\frac{-Q_d}{RT}\right\} \; and \; p = p_0 \exp\left\{\frac{-(Q_d + E_b)}{RT}\right\} \tag{2.2}$$

Here, k_0 and p_0 are constants, Q_d is the activation energy for diffusion, and E_b is the trap binding energy. Table 2.1 provides the binding energies associated with different hydrogen trap sites.

Microalloying elements like V help in grain refinement and improvement in strength through precipitate strengthening; V precipitates also play a role in hydrogen trapping. Malard *et al.* [33] performed a neutron scattering study of Fe-0.6C-18.14Mn-0.215V austenitic TWIP steel in 0.1 M aqueous NaOH solution. They observed no interaction between hydrogen and V in solid solution but did observe interaction with VC precipitates, which implies that they serve as hydrogen traps. Hydrogen content was measured using melt extraction, wherein 5 ppm wt. of H was not reversible even after heating the sample to 150 °C, which implies that precipitates act as a stable hydrogen trap. Dong *et al.* [34] observed better hydrogen resistance in V-microalloyed Fe-18Mn-0.6C-0.215V steel compared to base Fe-18Mn-0.6C.

Table 2.1: Hydrogen Trap Sites and Corresponding Binding Energies ($kJ \cdot mol^{-1}$)

Trap Type	Binding energy ($kJ \cdot mol^{-1}$)	Reference
Dislocation	20-59	21-24
Grain boundary	18-59	22-23,25-26
MnS interface	72	27-29
Cr, Mo or V atom	26-27	16,30
γ /α interface	52	31
V_4C_3	33–35	32
Mn atom	11	30

2.1.3. Influence of Hydrogen on Fracture

The influence of hydrogen embrittlement on austenitic steels can be determined by observing the fracture surface. The fracture for non-hydrogen charged conditions or alloys with excellent hydrogen embrittlement resistance is ductile (microvoid coalescence). In contrast, alloys with poor hydrogen resistance have brittle features (transgranular or intergranular) when tested in a hydrogen environment [45,94,95]. Figure 2.3 shows a schematic diagram of a typical fracture surface (using cathodic hydrogen charging) of austenitic alloys having poor hydrogen performance. Brittle fracture is shown on the outermost ring, and ductile features (unaffected dimple zone) are observed in the center. The location (surface or center region) of the brittle features on the fracture surface also depends on the hydrogen charging methodology, which is discussed later in this chapter. Koyama *et al.* [96] analyzed a Fe-18Mn-0.6C (wt. pct) steel using cathodic charging (in 3 pct. a NaCl aqueous solution containing 3 g·L of NH_4SCN at a current density of 10 $A \cdot m^2$). Ductile features like dimples can be observed in Figure 2.4 (a) in non-charged conditions. Figure 2.4 (b) shows the fracture surface in the hydrogen charged condition, with the highlighted area indicating the hydrogen-affected zone. Intergranular fracture (brittle feature) can be seen at high magnification from the same region in Figure 2.4 (c), and an unaffected dimple region can be observed at the center of the specimen (Figure 2.4 (d)). The hydrogen concentration is large near the surface, which explains the brittle behavior in the periphery region.

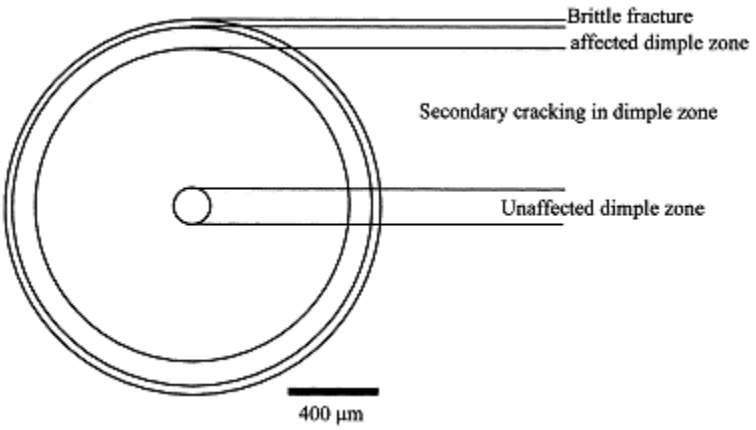

Figure 2.3: Schematic diagram of fracture surface observed after a cathodic charging hydrogen embrittlement experiment [94].

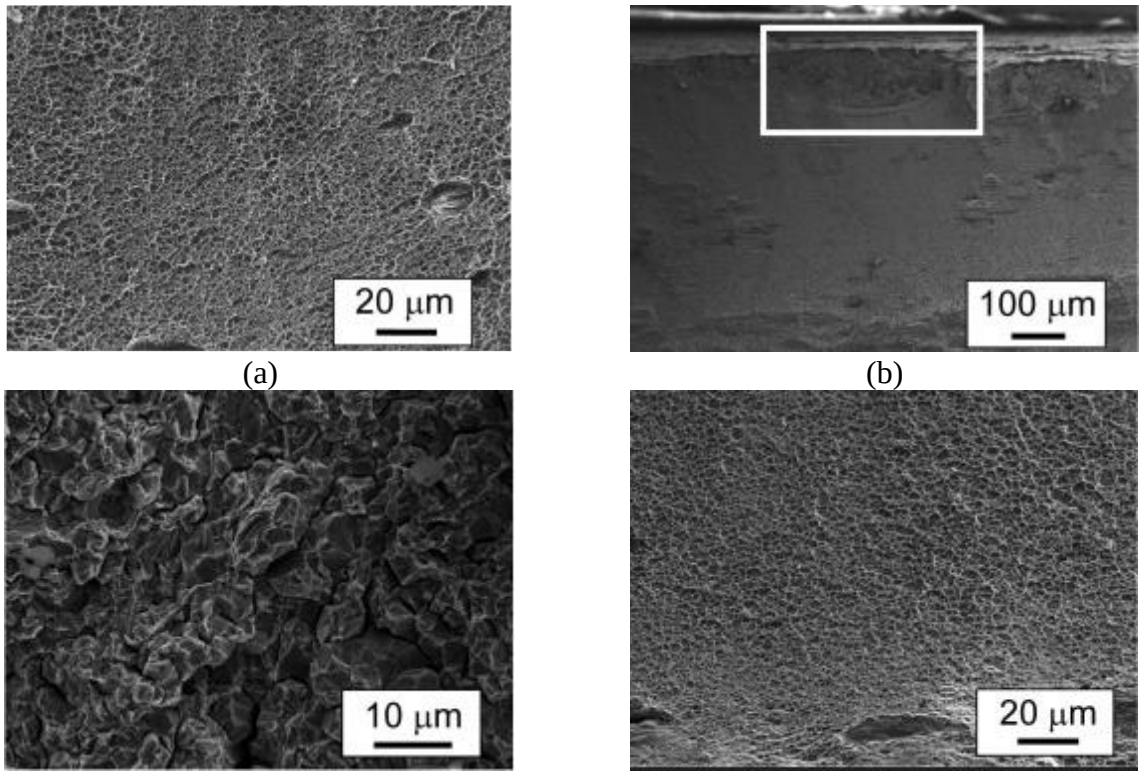

(a) (b)

(c) (d)

Figure 2.4: SEM images of Fe-18Mn-0.6C (wt. pct.) in (a) the non-charged condition and (b) Hydrogen charged condition with the box indicating brittle fracture, (c) high Magnification of the brittle fracture (surface of the specimen), and (d) high Magnification of ductile fracture (center of the specimens) [96].

2.2. Stacking Fault Energy (SFE) influence on Deformation Behavior of Austenitic Steels

SFE is the energy required to interrupt the regular sequence of atomic planes on a closed-packed crystal structure. FCC metals have two types of stacking faults: intrinsic and extrinsic. Figure 2.5 (a) schematically shows an intrinsic stacking fault, where part of the C layer has been removed, resulting in the interruption of the sequence. In Figure 2.5 (b), an extra A layer has been added between B and C, which might be termed as an extrinsic stacking fault [40]. Researchers [42-44], when referring to SFE of austenitic alloys, typically mean the intrinsic type. Figure 2.6 shows that alloys with SFE below 40 $mJ \cdot m^{-2}$ exhibits twinning induced plasticity and transformation induced plasticity ($\gamma \rightarrow \varepsilon$). These deformation mechanisms promote planar slip mechanisms, due to which the hydrogen interacts with dislocations at barriers such as grain boundaries leading to hydrogen failure. When the SFE is above 40 $mJ \cdot m^{2}$, perfect dislocation glide becomes the dominant deformation mechanism for austenitic alloys. In addition, cross-slip is easier at a higher stacking fault energy, which reduces the probability of both slip localization and hydrogen induced boundary separation [45-47].

Gibbs *et al.* [52] observed a threshold SFE value of 39 $mJ \cdot m^{-2}$ above which austenitic stainless steels (300 series) and Mn-stabilized alloys had a relative reduction in area (RRA) of above 80 pct, as shown in Figure 2.7. RRA is the ratio of reduction of area (RA) in hydrogen charged to that of air.

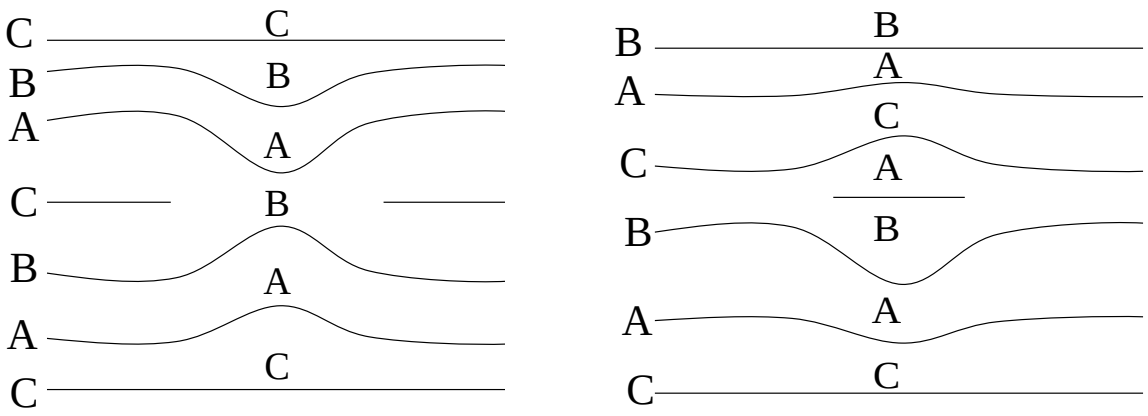

Figure 2.5: Schematic representation of (a) intrinsic and (b) extrinsic stacking fault types [40].

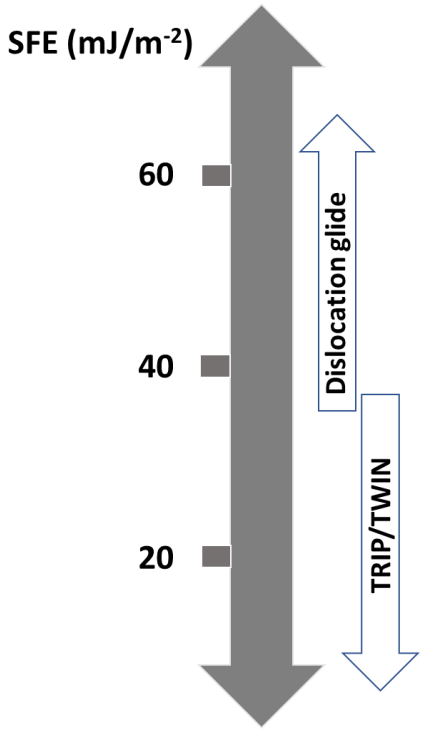

Figure 2.6: Schematic indicating deformation mechanism associated with various SFE ranges in austenitic steels [39].

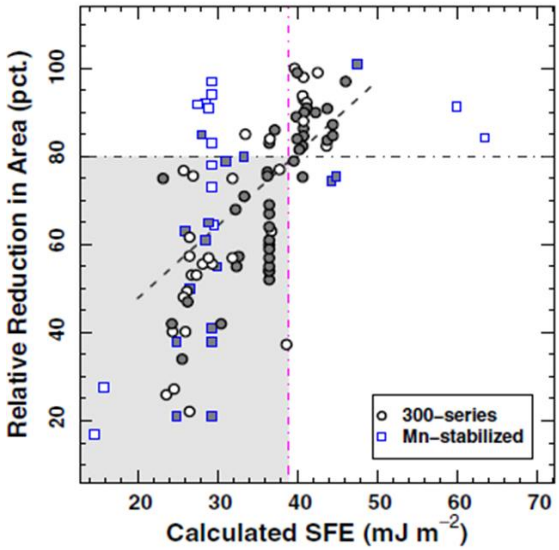

Figure 2.7: RRA plotted against calculated SFE for various austenitic steels. The horizontal line denotes an RRA value of 80 pct, which is cited as having acceptable performance in hydrogen. The vertical line indicates the SFE above which most alloys have an RRA above this threshold value [52].

2.2.1. Thermodynamic Modelling of SFE

A thermodynamic model for SFE was proposed by Olson and Adler [48-49], based on equation 2.3:

$$\gamma_{SFE} = 2\rho\,(\Delta G^{\gamma\rightarrow\varepsilon}) + 2\sigma \tag{2.3}$$

where γ_{SFE} is the intrinsic SFE, $\Delta G^{\gamma\rightarrow\varepsilon}$ is the Gibbs free energy of austenite (γ) to ε-martensite phase transformation, σ is the interfacial energy per unit area of the phase boundary, and ρ is the molar surface density of the closed-packed plane (*i.e.* {111} plane for austenite). The molar surface density, ρ, is obtained by following the equation given by Allain *et al.* [50]

$$\rho = \frac{4}{\sqrt{3}}\frac{1}{N_A(\alpha_\gamma{}^T)^2} \tag{2.4}$$

Here, N_A is the Avogadro's number. The variable $\alpha_\gamma{}^T$ is the composition dependent austenite lattice parameter and can be computed using the following equation provided by Babu *et al.* [54] and Saeed-Akbari *et al.* [43]

$$\begin{aligned}\alpha_\gamma{}^{300K} = {} & 3.5780 + 0.033X_C + 0.00095X_{Mn} - 0.0002X_{Ni} + 0.0006X_{Cr} \\ & + 0.0056X_{Al} + 0.0031X_{Mo} + 0.0018X_V\end{aligned} \tag{2.5}$$

Here, X_i is the molar fraction of the elements i in the system. Garcia de Andres *et al.* [100] proposed an equation to account for the temperature influence on austenite lattice parameter, which is given by:

$$\alpha_\gamma{}^T = \alpha_\gamma{}^{300K}[1 + \delta_y(T - 300)] \tag{2.6}$$

where, δ_y is the coefficient of thermal expansion of austenite and T is the temperature in Kelvin.

The equation to compute $\Delta G^{\gamma\rightarrow\varepsilon}$ is proposed by Gibbs *et al.* [52], dividing the driving force parameter in different components which are given below

$$\Delta G^{\gamma\rightarrow\varepsilon} = \Delta G^{\gamma\rightarrow\varepsilon}{}_{Chem} + \Delta G^{\gamma\rightarrow\varepsilon}{}_{Mag.} + \Delta G^{\gamma\rightarrow\varepsilon}{}_{GS} + \Delta G^{\gamma\rightarrow\varepsilon}{}_{Strain} \tag{2.7}$$

where, $\Delta G^{\gamma\rightarrow\varepsilon}{}_{Chem}$ is the driving force for chemical potential, $\Delta G^{\gamma\rightarrow\varepsilon}{}_{Mag}$ is the driving force due to the magnetism of the phases, $\Delta G^{\gamma\rightarrow\varepsilon}{}_{Strain}$ is associated with the strain induced due to change in crystallography and lattice parameter, $\Delta G^{\gamma\rightarrow\varepsilon}{}_{GS}$ is the driving force due to grain size. Gibbs *et al.* [52] suggested neglecting the strain and the grain size components on the basis of the previous work of Olson *et al.* [49], Takaki *et al.* [54] and Jun *et al.* [55]. Olson *et al.* [49] computed that $\Delta G^{\gamma\rightarrow\varepsilon}{}_{Strain}$ has a 0.1 pct. contribution to SFE. Takaki *et al.* [54] and Jun *et al.* [55] found that austenitic alloys with grain sizes of less than 30 μm have a minimal influence on the SFE.

$\Delta G^{\gamma\rightarrow\varepsilon}{}_{Chem}$ is given by [50,54]:

$$\Delta G^{\gamma\rightarrow\varepsilon}{}_{Chem} = \sum_{i} X_i \Delta G_i^{\gamma\rightarrow\varepsilon} + \sum_{ij} X_i X_j \Omega_{ij}^{\gamma\rightarrow\varepsilon} \tag{2.8}$$

where $G_i^{\gamma\rightarrow\varepsilon}$ is the element contribution to the driving force for transformation in an austenitic alloy system, $\Omega_{ij}^{\gamma\rightarrow\varepsilon}$ is the entropic interaction due to interactions of elements *i* and *j*, X_i and X_j are the molar fractions of the element *i* and *j* in the system. Functions associated with $G_i^{\gamma\rightarrow\varepsilon}$ and $\Omega_{ij}^{\gamma\rightarrow\varepsilon}$ for typical alloying elements are given in Table 2.2, where T is temperature in Kelvin. Researchers [43-44, 60-61] have developed a methodology to compute $\Delta G^{\gamma\rightarrow\varepsilon}{}_{Mag.}$ which is associated with the transition from the paramagnetic to antiferromagnetic state given by

$$\Delta G^{\gamma\rightarrow\varepsilon}{}_{Mag.} = \Delta G^{\gamma}{}_{Mag.} - \Delta G^{\varepsilon}{}_{Mag.} \tag{2.9}$$

$\Delta G^{\varphi}{}_{Mag.}$ can be computed using

$$\Delta G^{\varphi}{}_{Mag.} = \mathrm{RT}\left(1 + \frac{\beta^{\varphi}}{\mu_B}\right) f(\tau^{\varphi}) \tag{2.10}$$

Here, R is the ideal gas constant, β^{φ} is the magnetic moment, μ_B is the Bohr magnetron, and $f(\tau^{\varphi})$ is a function of temperature of interest of each phase (φ) computed using the equation given below:

$$f(\tau^{\varphi}) = \frac{T}{T_{Neel}^{\varphi}} \tag{2.11}$$

Here, T is the temperature of interest, and T_{Neel}^{φ} is the Neel Temperature, which depends upon the phase and can be computed based on the works of Saeed-Akbari *et al*. [43]

Table 2.2: Relationship to determine Thermodynamic Effects as a function of Temperature

Parameter	Formulae ($J \cdot mol^{-1}$)	References
$\Delta G_{Fe}^{\gamma \to \varepsilon}$	– 2243.38 + 4.309T	44,56
$\Delta G_{Ni}^{\gamma \to \varepsilon}$	1046 +1.255T	53
$\Delta G_{Mn}^{\gamma \to \varepsilon}$	-1000+1.123T	53
$\Delta G_{Cr}^{\gamma \to \varepsilon}$	1370-0.163T	53,60
$\Delta G_{Al}^{\gamma \to \varepsilon}$	2800+5T	60
$\Omega_{FeNi}^{\gamma \to \varepsilon}$	2095	102
$\Omega_{FeCr}^{\gamma \to \varepsilon}$	2095	102
$\Omega_{CrNi}^{\gamma \to \varepsilon}$	4190	102

2.2.2. Effect of Alloying Elements on SFE

As reflected from the alloying effects on various thermodynamic parameters described in Section 2.2.1., alloying elements play an integral role in determining the SFE of austenitic alloys. Several alloying elements that critically influence SFE of a high Mn austenitic system are introduced below:

(a) Manganese

Hsu *et al.* [62] reported that Mn increases the SFE in Fe-Mn-Si alloys. Medvedeva *et al.* [63] observed a parabolic relationship between Mn per atomic pct. and SFE in high Mn transformation induced plasticity (TRIP) steels. They observed an increasing relationship between SFE and Mn content above 20 wt. using ab-initio simulation. pct. Similarly, Jin *et al.* [64] experimentally found a trend of an increase in SFE with increasing Mn content for the Fe-C-Mn alloy system. Das [65] did a neural network analysis using extensive literature data of SFE as a function of Mn content in austenitic steels. A significant effect of Mn on SFE is shown in Figure 2.8 (a).

b) Nickel

Murr [66], first proposed the link between the high SFE of Ni [~128 $mJ \cdot m^{-2}$] and the cross-slip behavior of various austenitic stainless steels strained to relatively low strains compared to low SFE steels. Lee *et al.* [67] analyzed Ni in the Fe-Mn-Al alloy system and found an increasing trend in SFE with increasing Ni content. Similarly, the increasing trend in SFE was

also found in Fe-Cr-Ni alloys by Ferreira *et al.* [68]. Figure 2.8 (b) indicates that the Ni influence on increasing SFE is as significant as that of Mn [65].

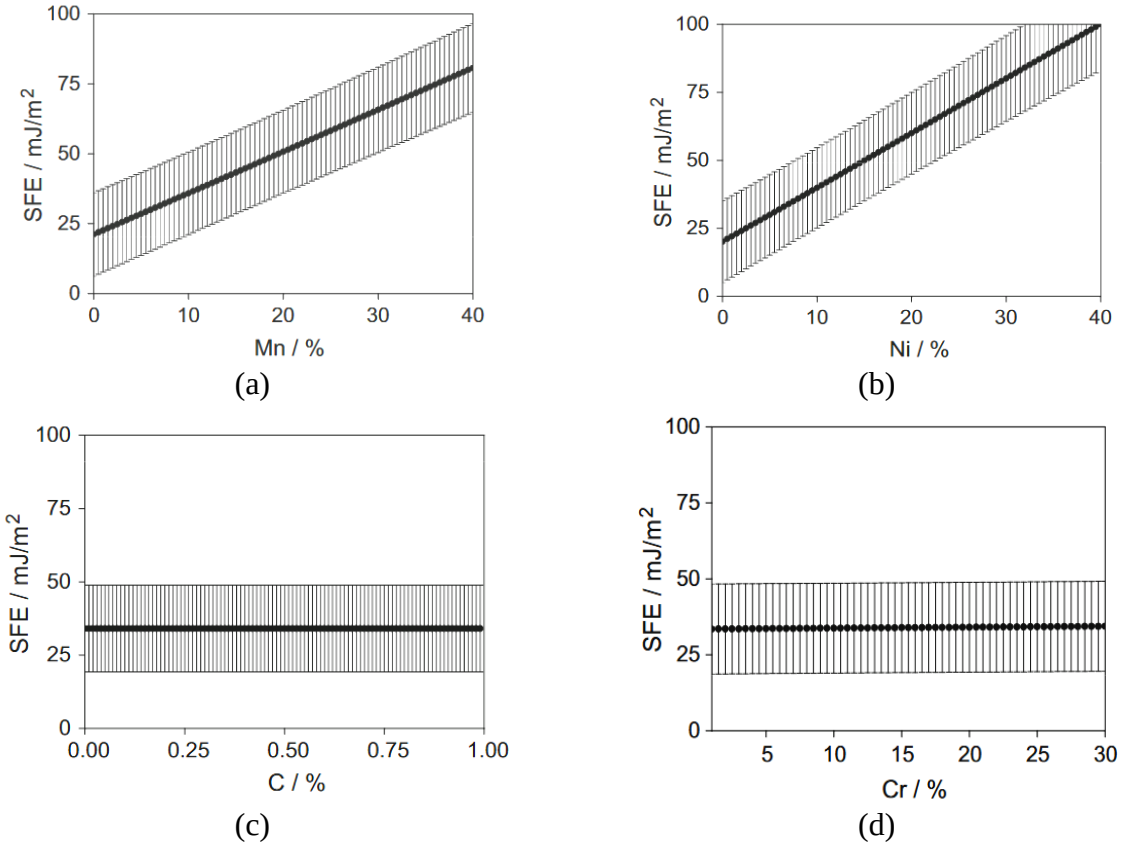

Figure 2.8: SFE in austenitic steels as a function of concentration of alloying elements: (a) Mn, (b) Ni, (c) C and. (d) Cr [65].

c) Carbon

Otto [69] suggested that SFE is not influenced by minor C content variations and observed that C might inhibit ε-martensite formation during deformation for Fe-Mn austenitic alloys.

Petrov *et al.* [70], based on theoretical calculations and experimental data, indicated that a low C content does not affect the SFE. However, at higher concentrations, C increases the SFE. As shown in Figure 2.8 (c), statistical analysis of the literature by Das indicated that SFE is generally independent of C content.

d) Chromium

Overall, there are conflicting results reported in the literature about the Cr effect on SFE

of austenitic steels. Das [65] reported that overall, Cr does *not* affect the SFE of austenitic alloys. In contrast, Prokoshkina *et al.* [71] observed that Cr in high N austenitic alloy lowers the SFE, interpreted from higher strain hardening (TWIP effect) in higher Cr conditions. Interestingly, Bracke *et al.* [72] argued that Cr increases SFE based on their observation of increased ductility for the Fe-Mn-Cr-C-N alloy system when compared against a Fe-Mn-C-N alloy, which implies cross-slip is the favorable mechanism. Figure 2.8 (d) indicates no change in SFE with increasing Cr content based on the statistical literature investigation [65].

e) Aluminum

Dumay *et al.* [42] suggested that Al increases the SFE in high Mn TWIP steel by observing the change in the deformation mechanism using X-ray diffraction. They observed cross slip in Al alloyed steel, whereas transformation-induced martensite was found in non-Al alloyed steel. Kim *et al.* [73] suggested a contrary behavior of Al due to it being a ferrite stabilizer. They explained that Al increases the martensite start (M_s) temperature, which promotes ε martensite formation.

2.3. Comparison of Stainless and High Mn Austenitic Steels

In general, 300 series austenitic stainless steels are expensive due to their high Ni content. A primary reason for Ni addition to these steels is to increase austenite stability. The strain induced martensite transformation contributes to poor hydrogen resistance in austenitic alloys [35-37]. 300 series stainless steels do not readily undergo strain-induced α' martensite transformation. Again, one primary drawback of use of austenitic stainless steels is the high material cost. Figure 2.9 shows that the price of Mn is substantially lower than the Ni throughout the highlighted timeline, which suggests that high Mn austenitic alloys may be a promising and cheaper alternative to the Ni-containing stainless steels.

A high Mn austenitic alloy has been reported to have comparable hydrogen performance to 316 stainless steel. For example, Figure 2.10 (a) presents the ultimate tensile strength as a function of test temperature for a high Mn austenitic steel (Fe-24.24Mn-0.46C-4.01Cr-0.02Ni-0.003Mo, all in wt. pct.) and 316L stainless steel in hydrogen charged versus non-charged conditions [38]. Both alloys have no significant strength degradation associated with hydrogen for the tested temperature range (-80 °C to 20 °C), suggesting equivalent hydrogen resistance between the high Mn steel and 316L stainless steel. The ductility of the high Mn austenitic steel over the temperature range is also comparable to that of 316L stainless steel, as shown in Figure

2.10 (b).

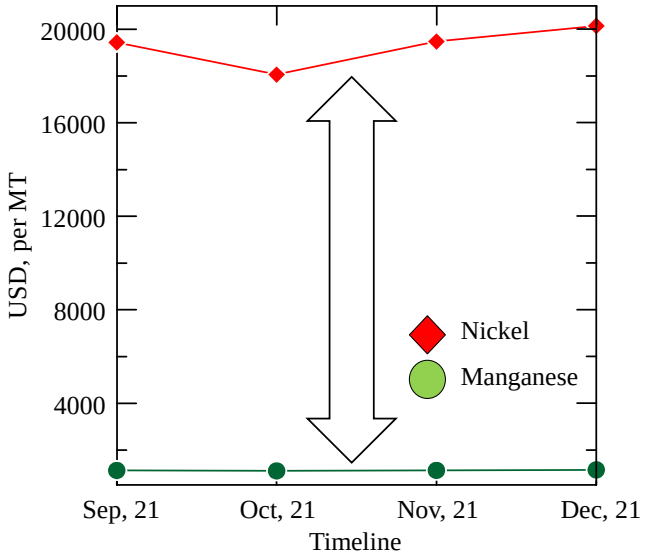

Figure 2.9: Prices of Ni and Mn per metric ton (MT) in 2021 [98].

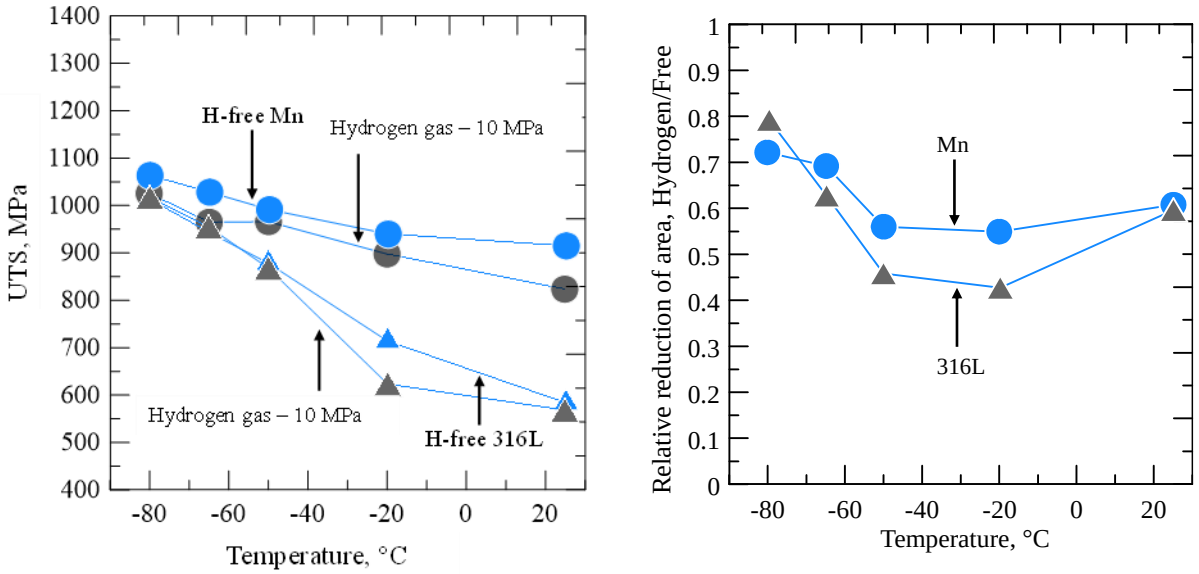

(a) (b)

Figure 2.10: (a) Ultimate tensile strength (UTS) as a function of test temperature for a high manganese (Mn) steel (Fe-24.24Mn-0.46C-4.01Cr-0.02Ni-0.003Mo, all in wt %) and a 316L stainless steel in hydrogen pre-charged and non-charged conditions. Hydrogen pre-charging was performed under a hydrogen gas pressure of 10 MPa at a temperature of 300 °C for 8 days (b) Relative reduction of area in hydrogen versus the air environment as a function of test temperature for high Mn and 316L stainless steels [38].

2.4. Strengthening Mechanisms in High Mn Alloys

Various strengthening mechanisms associated with the effects of grain refinement, precipitate strengthening, and alloying elements on the yield strength of high Mn austenitic steels are discussed below:

(a) Grain Refinement

Grain refinement is the primary strengthening mechanism for steels. Ueji *et al.* [79] studied the relationship between grain size and tensile properties for high Mn steel (Fe-22Mn-0.6C, all in wt pct). The yield and ultimate tensile strengths were the highest for a grain size of 1.8 μm and were the lowest for a grain size of 49.6 μm, as observed in Figure 2.11. This grain size effect on the yield strength of the alloys can be predicted using the Hall-Petch equation (2.10), where σ_0 is the materials constant for the starting stress for dislocation movement, k_y is the strengthening coefficient, and *d* is the grain diameter [97]

$$YS = \sigma_0 + \frac{k_y}{\sqrt{d}} \tag{2.10}$$

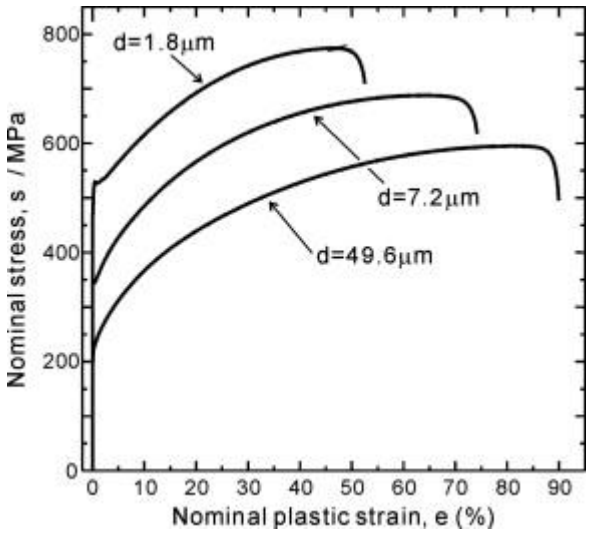

Figure 2.11: Engineering stress-strain curves of a high Mn austenitic steel (Fe-31Mn–3Al–3Si, all in wt pct) with different grain sizes. The mechanical properties are significantly influenced by grain size [79].

(b) Influence of Carbon and Manganese on Yield Strength

Bouaziz *et al.* [80] proposed an equation to predict the yield strength of high Mn austenitic steels considering the effects of C and Mn, which is given below:

$$\sigma_y\ (\text{MPa}) = 228 + 187\ (\text{wt pct C}) - 2(\text{wt pct Mn}) \tag{2.11}$$

Here σ_y is the yield strength. Eq. (2.11) reflects a strong effect of C on strengthening. C can influence the yield strength via Cottrell atmospheres [82]. In addition, C being an interstitial atom, interacts with dislocations that pile up at the grain boundaries and increases the strain hardening behavior of high Mn alloys [81]. Short range ordering (SRO) might help in understanding the influence of Mn. SRO is described as local order arising when the number of the unlike atom pairs is more significant than that in a random solution [83-84]. The attraction between C and Mn atoms might act as a hindrance to dislocation glide [83]. Multiple studies [85] have indicated that SRO in high Mn alloys might help in strengthening and work hardening.

(c) Precipitation Strengthening

Microalloying elements (Ti, V, and Nb) influence the grain refinement and precipitate strengthening of austenitic alloys. Scott *et al.* [86] investigated the influence of Ti, V, and Nb precipitates on mechanical properties of different compositions of high Mn austenitic steels: Fe-22Mn-0.6C, Fe-17Mn-0.9C, and Fe-18Mn-0.6C-0.9Al. The conditions were aged to promote precipitation. Figure 2.12 shows the influence of V, Ti, and Nb on the strength of the high Mn alloys. Below 0.2 wt. pct, Ti has a higher degree of strengthening, whereas, above that, V has a greater effect. The solubility of V is higher than Ti in austenite, which helps enable formation of finer VC precipitates. Ti at higher concentrations forms coarse TiC precipitates. Compared to Ti or V, Nb has a relatively insignificant strengthening effect. V microalloyed Fe-22Mn-0.6C and Fe-17Mn-0.9C alloys had similar strengthening trends, despite the considerable difference in carbon content.

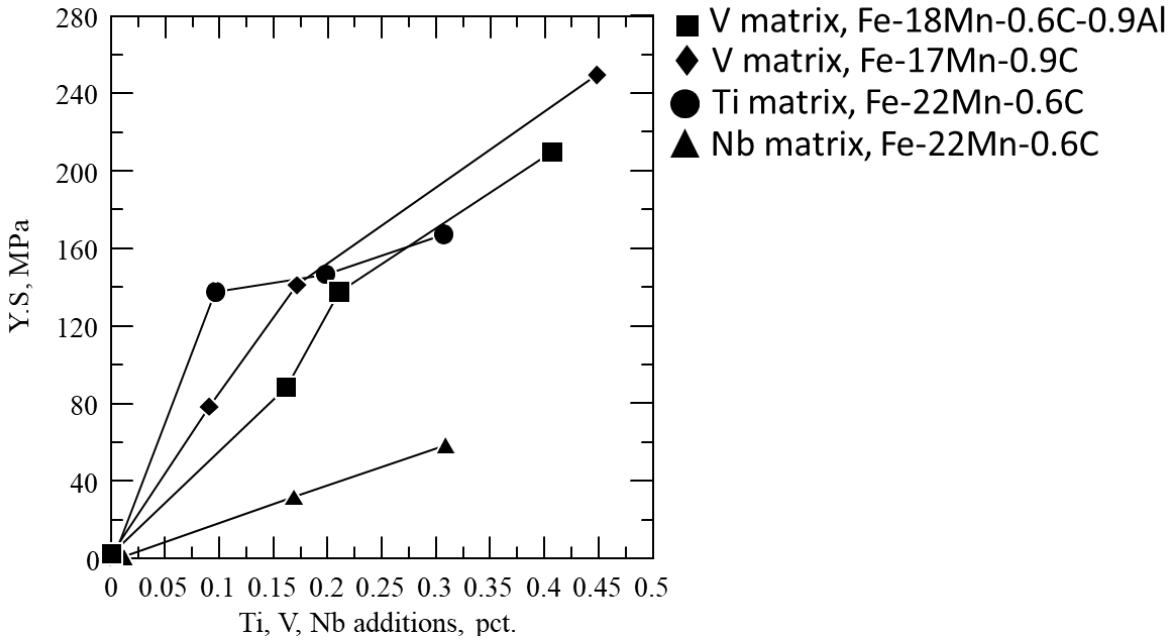

Figure 2.12: Yield strength plotted against microalloying element (Ti, V, and Nb) concentration for various high Mn austenitic steels [86].

2.5. Processing Routes for High Mn Alloys

Figure 2.13 shows the thermomechanical processing for hot-rolled and cold rolled austenitic steels. Fe-Mn-Al-C austenitic alloys are initially prepared as ingots using the melting and casting process. These types of alloys are homogenized between the temperatures of 1100 – 1250 °C and hot rolled to the desired thickness at a finish rolling temperature range of 850-1000 °C (multiple rolling passes during hot rolling are preferred to avoid cracking of the plates) [88]. Hot rolled slabs can be air or water-cooled. Homogenization is performed to reduce the negative effect of elemental segregation. Hot rolling in the single γ phase region results in recrystallization of the microstructure [89]. Isothermal annealing or aging may be applied to the hot rolled steel as indicated in Figure 2.13. A cold worked Fe-Mn-Al-C steel can be solution treated in the temperature range of 900-1000 °C and then quenched in water or any other media. Aging can be performed on cold worked steels, as shown in Figure 2.13. Cold working increases the dislocation density and, in conjunction with annealing, can generate recrystallization, leading to grain refinement [87].

San Marchi *et al.* [90] did a comparison study between annealed and strain hardened (cold worked) 316 and 316L stainless steel in the hydrogen charged condition (pre-charged in

138 MPa hydrogen gas for 10 days). Strain hardened and annealed alloys performed better in hydrogen-charged conditions compared to the non-charged condition as shown in Figure 2.14. Strain hardening increases the strength of austenitic alloys with no significant hydrogen embrittlement effects.

Aging, after hot rolling or cold rolling, is considered important for microalloyed steels to enhance strength through the formation of microalloy precipitates, like VC [91-92]. It is integral to control the cooling rate before and after aging, which may influence precipitate size and volume fraction, and thus the mechanical properties of high Mn alloys [93].

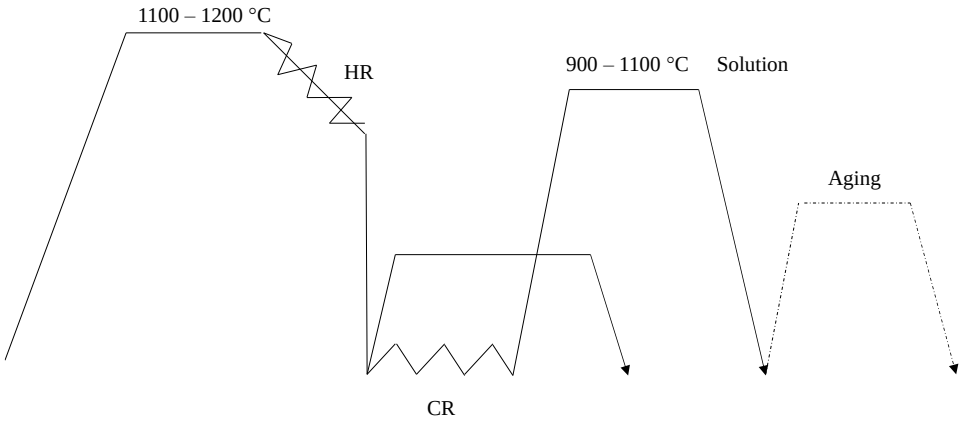

Figure 2.13: Thermomechanical processing schematic for hot-rolled and cold-rolled austenitic steels [88].

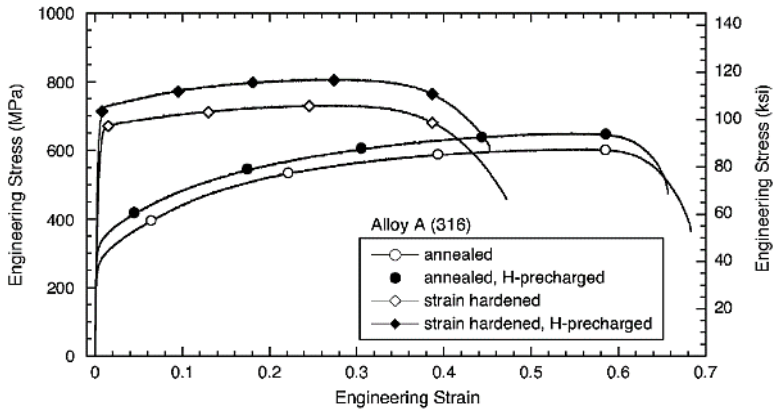

Figure 2.14: Engineering stress-strain curves for annealed and strain hardened (a) 316 and (b) 316L stainless steels in non-charged and H-charged conditions [90].

Figure 2.14: Continued

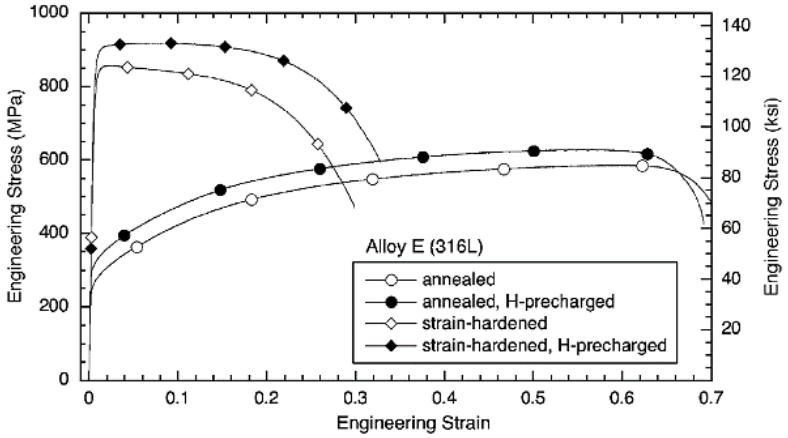

(b)

2.6. Hydrogen Charging Methodologies

Cathodic and gaseous hydrogen charging methods are commonly used to evaluate hydrogen embrittlement characteristics of a material. Cathodic charging is relatively more economical and widely accessible, whereas gaseous charging is expensive and less accessible but is more relevant to gaseous hydrogen service in practice.

Hydrogen embrittlement mechanisms are associated with hydrogen trapping and hydrogen concentration. The type of trap is determined based on activation energy. Irreversible traps require a higher activation energy for hydrogen desorption [75]. A discussion of activation energy is given in Section 2.1.2. Silverstein *et al.* [74] performed a comparison study between gaseous charging (3 h at 300 °C under 60 MPa hydrogen gas pressure - associated with low hydrogen fugacity) and cathodic charging (72 h in a 0.5 N H_2SO_4 solution with a current density of 50 $mA \cdot cm^{-2}$ associated with higher fugacity) for a duplex stainless steel. They observed that the gaseous charging method resulted in a much higher hydrogen trap (irreversible) activation energy (77 $kJ \cdot mol^{-1}$) compared to cathodic charging (63 $kJ \cdot mol^{-1}$). According to the authors, the variation in activation energy was due to the different degrees of hydrogen desorption. Figure 2.15 shows the quantity of hydrogen (wt. ppm) in duplex stainless steel after cathodic and gaseous charging; the hydrogen content is measured using a LECO® RH-404 hydrogen analyzer (measurement accuracy $\pm$ 0.5 wt. ppm). With different heating rates, cathodic charging for 72 hr has the highest hydrogen content evolution compared to gaseous charging, which insinuates that cathodic charging is more severe than gaseous charging.

Electrolytic solutions for cathodic charging are also an essential component for hydrogen embrittlement experiments. Conventionally, H_2SO_4 or NaOH aqueous solutions are most

commonly used as electrolytic solutions. Yoo *et al.* [76] analyzed hydrogen embrittlement characteristics of different alloys (low carbon and heat resistant Cr-Mo steels) tested using both 0.1 M NaOH and 0.5 M H_2SO_4 solutions with the same current density of 200 $A \cdot m^{-2}$. They observed that H_2SO_4 more severely embrittled the specimens compared to NaOH. Venezuela *et al.* [77] assert that hydrogen fugacity associated with the H_2SO_4 electrolyte is significantly higher compared to the NaOH electrolyte. Escobar *et al.* [78] did similar experiments for ferritic-bainitic steels, which indicated the more severe embrittlement effect of 0.5M H_2SO_4 is partly due to the difference in hydrogen concentration of the solution when compared to 0.1M NaOH. The pH levels can also explain the different embrittlement effects of these two solutions. NaOH, with strong basicity, has high pH, wherein the surface of the metal is not easily damaged and can even resist hydrogen penetration. However, H_2SO_4, with strong acidity, lowers the pH and damages the metal surface, thus helping in hydrogen penetration [75].

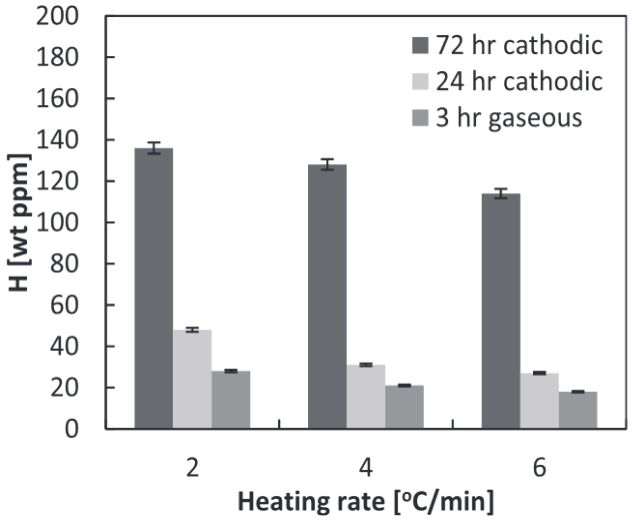

Figure 2.15: Hydrogen content plotted against heating rate using LECO® RH-404 hydrogen analyzer under different charging methodologies [74].

CHAPTER 3: EXPERIMENTAL DESIGN AND METHODS

3.1. Experimental Design

316L stainless steel was used as the reference austenitic alloy in this study as it represents high Ni austenitic alloy commonly utilized for hydrogen applications. The performance of different grades of high Mn alloys (H1 and H2) with regards to tensile strength and hydrogen embrittlement performance were used to design a new alloy.

The 316L stainless steel was obtained from Sandia National Laboratory. Two different grades of high Mn austenitic alloys (H1, H2) were acquired from POSCO. The designed V-microalloyed High Mn steel was melted and hot rolled by US Steel. The 316L stainless steel was in the form of a bar. The H1, H2 and designed V-microalloyed high Mn steel were in plate form.

The importance of SFE in hydrogen embrittlement resistance, methodology for thermodynamic modeling of SFE, and influence of individual alloying elements on the same have been discussed in Chapter 2. Table 3.1 shows the chemical composition of all the alloys studied in this project and their calculated SFE. The calculated SFE values for H1 and H2 were 28.9 and 49 $mJ \cdot m^{-2}$, respectively, indicating that H2 was above the threshold. The H2 alloy had significantly higher calculated SFE than H1, one of the reasons being the inclusion of Ni as an alloying element for H2. This calculation is based on the thermodynamics parameters given in Table 2.2. The effect of Cr was neglected in the present model due to contradicting literature related to Cr's influence on SFE (see Chapter 2.2). The SFE for 316L SS (40 $mJ \cdot m^{-2}$) was obtained from the work of Gibbs *et al.* [52]

The thermodynamic model used for this project is discussed in Chapter 2. The model used for this project was based on the works of Gibbs *et al*. [52], Saeed-Akbari *et al*. [43], Curtze *et al*. [100], and Yakubstov *et al.* [102]. The objective of using the model is to determine alloy compositions that would result in SFE values higher than the threshold (39 $mJ \cdot m^{-2}$) determined by Gibbs *et al* [52]. The influence of Mn and Al concentration on SFE of Fe-Mn-Al (wt. pct.) austenitic alloys is indicated in Figure 3.1. Both of these elements increase the SFE. The influence of only Al without Mn content on the SFE in austenitic steels is calculated to get the rate of SFE increase. Figure 3.2 shows the influence of Al in an Fe-0.2C-15Mn-*x*Al alloy; a minimum of 8-9 pct. of Al has to be added to the alloy system to maintain the threshold SFE. However, the amount of Al can be lowered by increasing Mn content. The contribution of Mn content to SFE is higher than Al according to the thermodynamic model used in this study.

The addition of C in a high Mn alloys increases SFE for a constant Mn content in an Fe-*x*Mn-*y*C alloy system, as shown in Figure 3.3. A minimum of 0.6 wt. pct. of C and 27-30 wt. pct. Mn are required to exceed the threshold SFE (~39 $mJ \cdot m^{-2}$).

The thermodynamic model used in this project for computing SFE is compared against different models by Saeed-Akbari *et al.* [43] and Dumay *et al.* [42]. The focus of these comparisons is on high Mn alloys and to verify that the model used for this project doesn't have massive deviations from the literature. The alloy compositions analyzed in this analysis were high Mn austenitic steels, with C and Al additions. Table 3.2 shows the compositions of Fe-*x*C-*y*Mn-*z*Al alloys evaluated for comparison. Figure 3.4 illustrates the SFE values of the present model compared to other models. The average difference in SFE between Dumay *et al.* [42] and the present model is 7.66 $mJ \cdot m^{-2}$. The average difference between Saeed-Akbari *et al.* [43] and present model is 3.74 $mJ \cdot m^{-2}$. The present model used for this project demonstrates better correspondence with the model by Saeed-Akbari *et al*. The difference between the models can be attributed to assumptions or thermodynamic parameters used for this calculation. The interfacial energy (σ) and $\Delta G^{\gamma \rightarrow \varepsilon}{}_{Chem}$ were different for each model [99-102], which explains the SFE variation.

The thermodynamic model for this project was assessed against experimental values of SFE. The experimental values were acquired either using X-ray diffraction or transmission electron microscopy [103]. The comparisons aim to verify that the deviations of SFEs between experimental and thermodynamic are within an acceptable range. Table 3.3 describes the composition of austenitic alloys for which experimental SFE values are available in the literature. Figure 3.5 shows the comparison between calculated and experimental SFE. The average difference between calculated and experimental SFE is computed to be 10.2 $mJ \cdot m^{-2}$, which is relatively high and implies that the calculated SFE overpredicts the experimental values. The composition of the designed V-microalloyed high Mn steel is selected to achieve a significantly higher SFE than the threshold (39 $mJ \cdot m^{-2}$) to overcome the experimental and calculated differences.

Similar to H2, the alloy developed in this study was designed to have high Mn, Al, and a limited concentration of Ni to obtain a high SFE. 0.25 wt. pct. of C is added for strength contribution without increasing the brittleness of the alloy. 0.25 wt. pct. of V is added for grain refinement during hot rolling and precipitate strengthening during aging. In this thesis, this steel will be termed as V-microalloyed high Mn steel. Table 3.4 indicates the proposed and actual alloy composition of the designed V-microalloyed high Mn steel with corresponding SFE, calculated by the thermodynamic model.

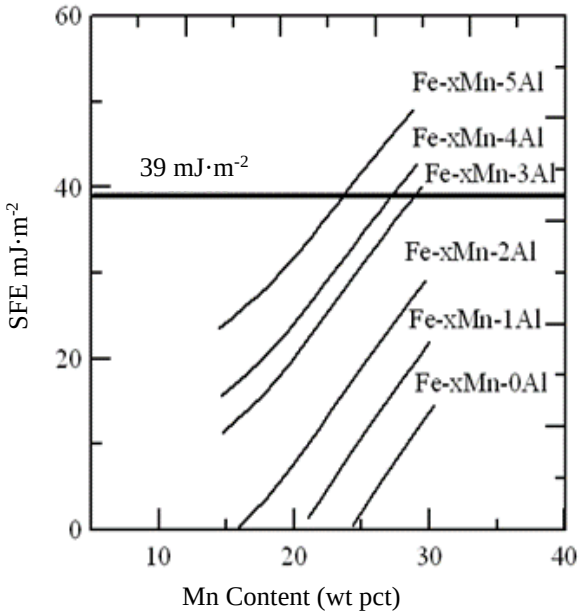

Figure 3.1: Effects of Al and Mn concentrations on the SFE of austenitic Fe-*x*Mn-*y*Al alloys (in wt pct). Only positive values of SFE are indicated.

Table 3.1: Chemical Compositions and Calculated SFE of POSCO-Produced High Mn Alloys (H1 and H2), 316L Stainless Steel, and V-microalloyed High Mn Steel (wt pct)

Alloy	C	Mn	Si	Cr	Al	N	Nb	Ti	Ni	V	SFE ($mJ \cdot m^{-2}$)
316L Stainless Steel	0.017	1.25	0.59	17.57	-	0.048	0.03	0.002	12.97	-	~ 40 [52]
H1 (POSCO)	0.24	30.0	-	2.73	-	-	-	-	-	-	28.9
H2 (POSCO)	0.25	30.4	-	2.71	1.75	-	-	-	3.0	-	49.0
V-microalloyed High Mn Steel (US Steel)	0.262	29.6	-	-	1.66	-	-	-	2.87	0.243	47.3

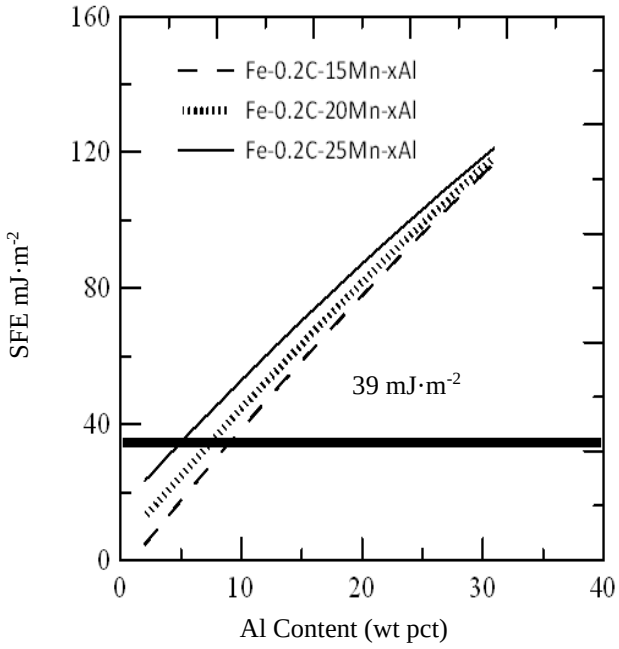

Figure 3.2: Effects of Al and Mn concentrations on the SFE of austenitic Fe-0.2C-*x*Mn-*y*Al (wt pct) alloys.

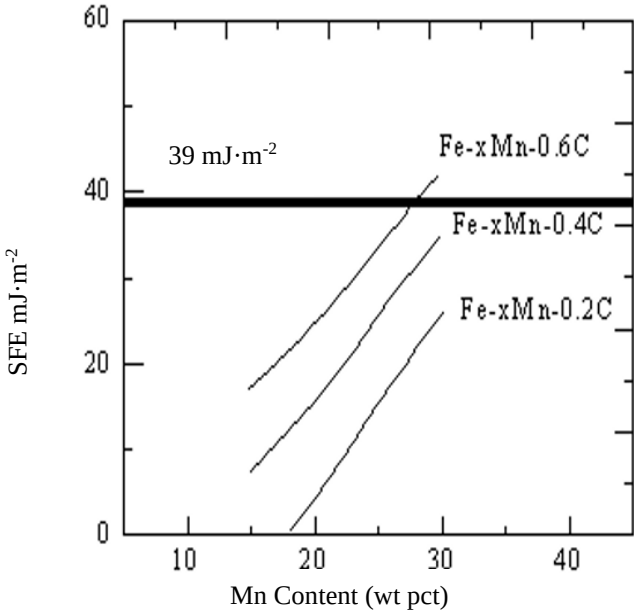

Figure 3.3: Effect of C and Mn concentration on the SFE in austenitic Fe-*x*Mn-*y*C (wt pct) alloys.

Table 3.2: Chemical Composition of Alloys Shown in Figure 3.5 (wt pct)

Number	Alloys
1	Fe-18Mn-0.6C
2	Fe-18Mn-0.6C-1.5Al
3	Fe-18Mn-0.6C-2Al
4	Fe-15Mn-0.6C
5	Fe-15Mn-0.6C-1.5Al
6	Fe-15Mn-0.6C-2Al
7	Fe-12Mn-0.6C
8	Fe-12Mn-0.6C-1.5Al
9	Fe-12Mn-0.6C-2Al

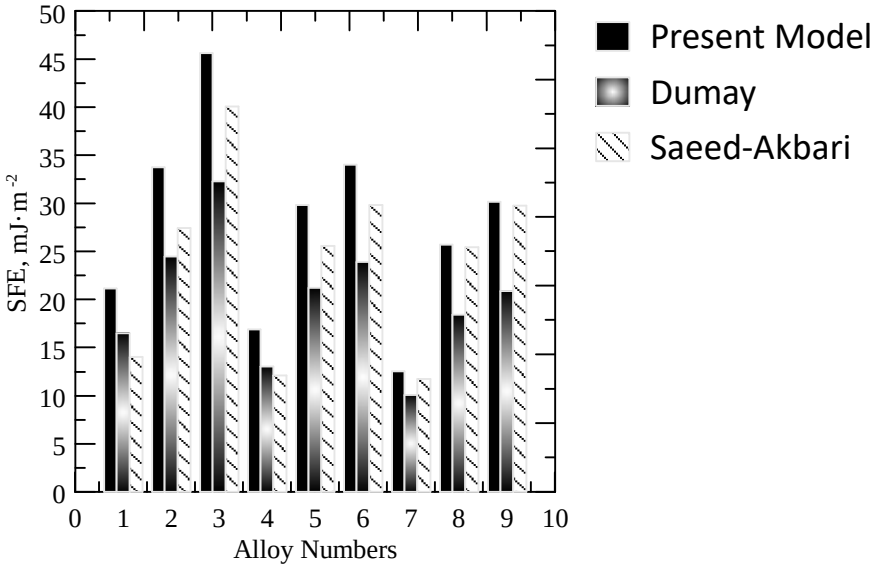

Figure 3.4: Comparison of SFE calculated using different thermodynamic models with the present calculation. The SFE obtained based on a thermodynamic model in this work are shown. The SFE calculated using the thermodynamic modeling by Dumay *et al.* [42] and Saeed-Akbari *et al.* [43] are also shown.

Table 3.3: Chemical Composition of Alloys for Experimental-Model SFE Comparison (wt pct)

Number	Alloys
1	Fe-25Mn-0.15C-0.6Al
2	Fe-25Mn-0.15C-1.5Al
3	Fe-25Mn-0.1C-2.2Al
4	Fe-25Mn-0.15C-3.1Al
5	Fe-25Mn-0.15C-4.8Al
6	Fe-31Mn-0.17C-2Al

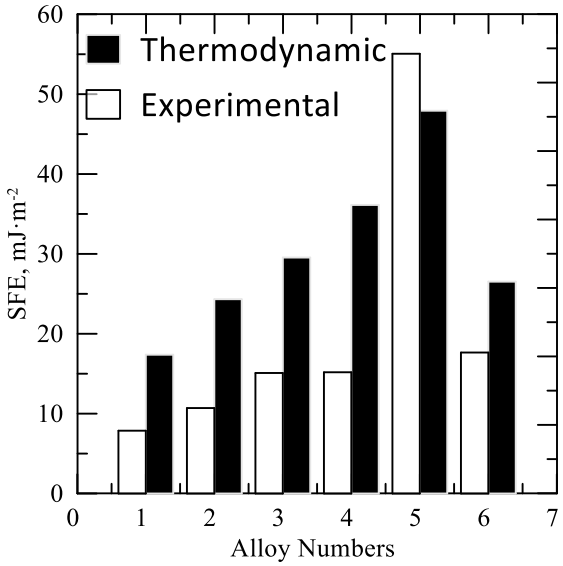

Figure 3.5: Comparison of SFE values measured experimentally versus calculated using a thermodynamic model in this work [103].

Table 3.4: Target and Actual Chemical Compositions of the Newly Designed V-Microalloyed High Mn Austenitic Alloy (wt pct)

Alloy	C	Mn	Al	Ni	V	SFE ($mJ \cdot m^{-2}$)
Proposed	0.25	30.0	1.75	3.0	0.25	48.3
Actual	0.262	29.6	1.66	2.87	0.243	47.3

3.2. Processing of V-microalloyed High Mn Steel

The homogenization process of the V-microalloyed high Mn steel preceding hot rolling was performed at a temperature of around 1200°C for 2 hours. Figure 3.6 shows a pseudo-binary phase diagram for an Fe-*x*C -29.6Mn-1.66Al-2.87Ni-0.243V alloy (in wt. pct) associated with the designed alloy composition. Per the phase diagram, the hot (and finish) rolling temperature is selected to be above 850 °C so that the steel is hot-rolled in the austenite single phase field (FCC_A1) without forming VC precipitates, thus keeping V in solution to allow for greater precipitation strengthening potential during subsequent aging.

Figure 3.7 shows a schematic of the thermo-mechanical process used for the designed V-microalloyed high Mn alloy. The proposed finish rolling temperature was 900 °C, but the actual temperature was 1000 °C. The hot rolled designed alloy was rapidly cooled to room temperature using water. The designed V-microalloyed high Mn steel was hot rolled by US Steel. The

dimensions of the as-received hot rolled plates were 406 mm in length, 203 mm in width, and 15 mm in thickness.

Cold working and aging of the designed alloys were performed at Mines to increase strength and evaluate the role of processing on hydrogen embrittlement. A level of 20-pct. cold working was selected according to the tensile test results (strength/elongation) of the hot rolled V-microalloyed high Mn steel. The hot rolled V-microalloyed high Mn steel had very high ductility, due to which 20 pct cold working post-processing parameter was selected without significantly impacting its elongation parameter. The specimens for the evolution of hardness and aging were cut from the base plate in the shape of coupons with dimensions of approximately 25 mm×25 mm×15 mm. The specimens were cold rolled using the Fenn® rolling mill at Mines.

The objective of aging was to achieve VC precipitates for strength enhancement. The V-containing precipitates associated with MC (FCC_A1#2) in the phase diagram shown in the Figure 3.6 are thermodynamically stable at temperatures ranging from 300 to 850 °C at a C content of 0.262 wt. pct. The heat treatments for the aging of V-microalloyed high Mn steel were performed in a box furnace. The temperatures for heat treatments ranged from 300 to 700 °C for holding times of 30 minutes, 1 hour, 2 hours, 5 hours, and 10 hours. The specimens were cut from the base plate in coupons with dimensions of approximately 25 mm×25 mm×15 mm. The specimen temperatures in the box furnace were monitored using a thermocouple connected to the specimen surface. There was a variation of approximately ±10 °C between the programmed and actual temperature of the specimen. The specimens were water quenched after aging.

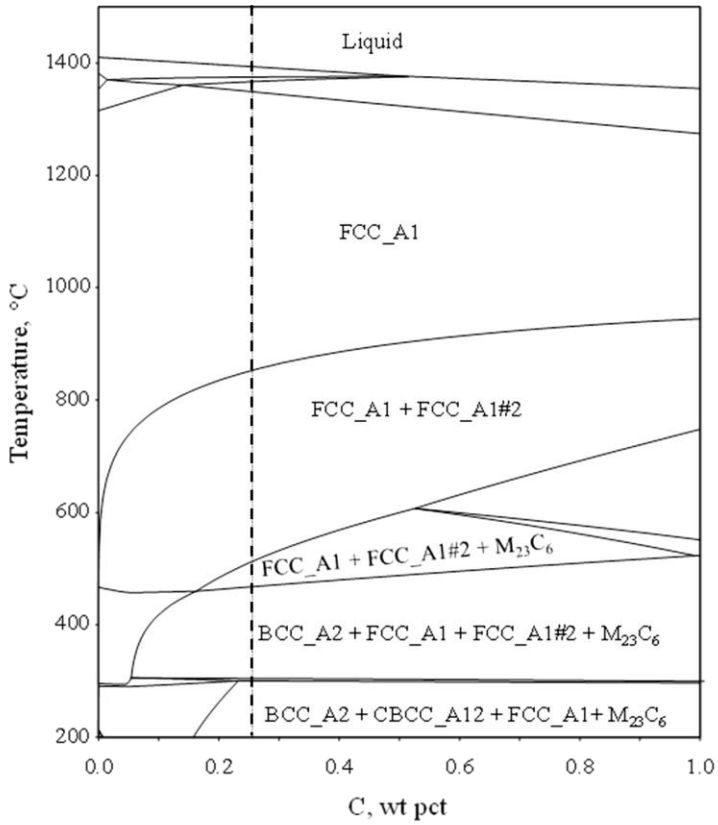

Figure 3.6: Pseudo-binary phase diagram for an Fe-*x*C-29.6Mn-1.66Al-2.87Ni-0.243V alloy (in wt pct) associated with the designed alloy composition. FCC_Al: γ-austenite, FCC_A1#2: MC or vanadium carbide, BCC_A2: α-ferrite, and CBCC_A12: pure α-Mn. The condition with a carbon content of 0.262 wt pct, matching the actual composition of the designed alloy used in this study, is indicated by a dashed line.

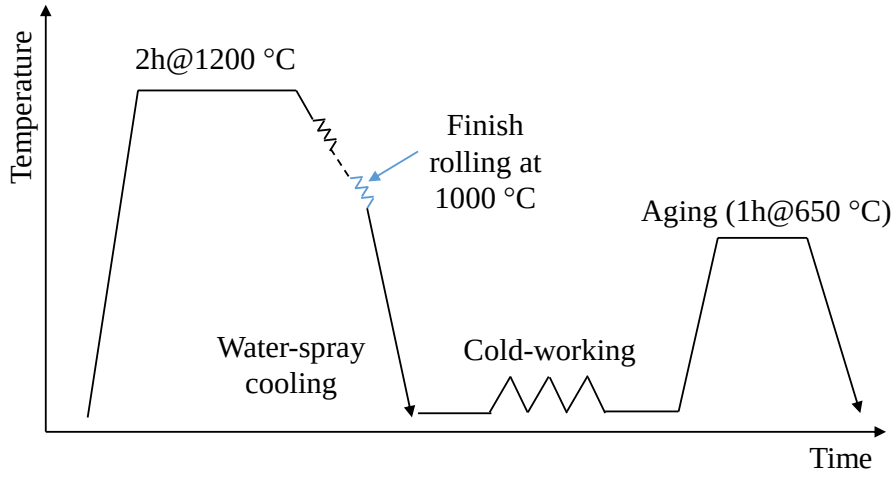

Figure 3.7: Processing route used for the designed V-microalloyed high Mn austenitic steel, produced at US Steel.

3.3. Metallography and Characterization

The specimens for metallography were sectioned in the as-received and post processed conditions such that the RD-ND plane corresponds to the polish plane. They were mechanically ground utilizing SiC paper with grit sizes of 400, 600, 800, and 1200. After grinding, they were polished using diamond media ranging from 3 to 1 μm. Further, Vibro-met polishing was performed to remove micro-scratches and deformation. The specimens were etched using 4 pct. Nital. Microstructure analysis was carried out using light optical microscopy. The grain size of the alloys was determined according to the methodology given in ASTM E112 [105].

The phase stability of austenite is integral to having high hydrogen embrittlement resistance. The specimens for the evaluation of phase stability were cut into 8-10 mm sections, including the fracture surface from tensile samples. They were cross-sectioned along the longitudinal direction. The grinding and polishing steps were the same as above used for metallography. The analysis of phase stability or strain induced martensitic transformation in the alloys was performed using X-ray diffraction (XRD). The scans were performed on a PANalytical PW3040 X-ray Diffractometer with Cu Kα radiation with 2θ° ranging from 40 to 90°. Further analysis of the phase stability was evaluated using electron backscatter diffraction (EBSD). EBSD was conducted using a FEI Helios Nanolab 600i SEM/FIB.

3.4. Hardness Measurement Methodology

The strength enhancement of the cold worked and aged specimens were analyzed using hardness testing. The hardness was determined using a LECO® AMH55 Automated Hardness Indenter. The load used for the hardness study was 500 gf, and nine data points were used to determine the average hardness value.

3.5. Mechanical Testing

3.5.1. Sample Preparation

The tensile blanks (for cold working and aging) and specimens were machined direction using electrical discharge machining, such that the tensile axis is parallel to the rolling direction of the plates. The schematic drawing of the sub-size tensile specimens is shown in Figure 3.8.

The circular notch tensile (CNT) specimens were machined from the H1 and H2 alloys by electrical discharge machining such that the tensile axis is parallel to the longitudinal direction. As the plated were curvature in nature along the rolling direction.

The circular notch tensile (CNT) specimens were machined in the rolling direction from the plates. Two types of CNT geometries were machined for hydrogen embrittlement experiments. The two CNT geometries can be termed as ‘large’ and ‘small’ CNT due to the difference in the diameter. The as-received conditions were tested using large CNT specimens. The specimen geometry for tensile and ‘large’ CNT specimens was based on the work of Kagay [104]. The ‘small’ CNT geometry was based on the specimen geometry typically used for hydrogen embrittlement testing in gaseous environments at SNL. In the present case, the cold worked and cold worked + aged conditions were examined using small CNT specimens for hydrogen embrittlement due to the thickness constraint of the cold-rolled tensile blanks. The drawings of both small and large CNT specimens are shown in Figures 3.9 and 3.10, respectively.

3.5.2. Tensile Testing

The tensile tests were performed on an Instru-met® load frame with an engineering strain rate of 5.0×10^{-4} s^{-1}. The displacement was measured using a 25.4 mm gauge length extensometer.

3.5.3. Hydrogen Embrittlement Testing

The hydrogen embrittlement susceptibility of the alloys was studied by *in-situ* mechanical testing (rising displacement testing using a constant displacement rate of 0.005 $mm \cdot min^{-1}$ (0.0002 $in \cdot min^{-1}$) with a direct current potential drop (DCPD) method to measure crack growth. These tests were performed while cathodically charging a specimen with hydrogen. Circumferentially notched tensile (CNT) specimens were cathodically charged using a 0.05 M NaOH aqueous charging solution and current density of 1.65 $mA \cdot cm^{-2}$ in an acrylic environmental chamber [106]. During the testing, argon gas was bubbled into the aqueous solution to remove oxygen and stir the solution. Two mixed-metal oxide electrodes were placed on either side of the CNT specimen with current supplied by a programmable direct current power supply [104].

The stress values were obtained after dividing the load by the original cross-sectional area of the notched region. In preliminary experiments, cathodic hydrogen charging was performed using an H_2SO_4-based aqueous solution, but it resulted in significant corrosion of the sample surface. The cathodic charging solution was changed to a NaOH-based solution, which was found *not* to cause such corrosion during hydrogen charging experiments. The apparatus for hydrogen embrittlement mechanical testing is shown in Figure 3.11. The same displacement rate parameters were used in air for comparison with the hydrogen charged condition.

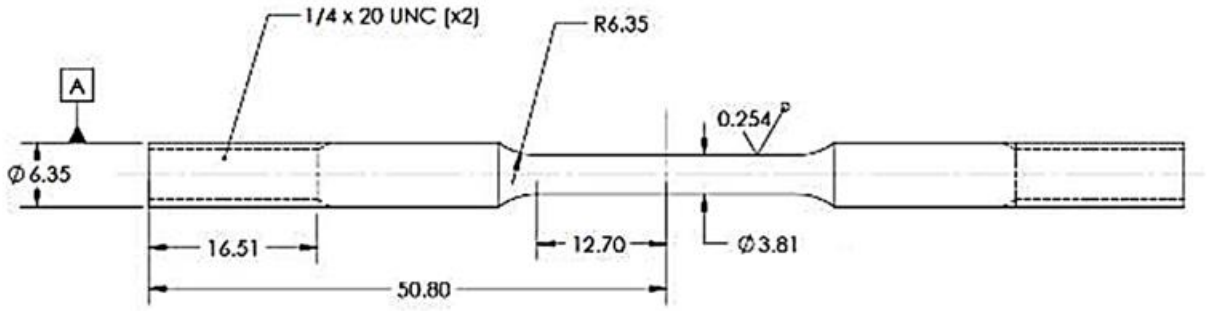

Figure 3.8: Drawing of subsize tensile specimen. Dimensions are in mm except for surface finish (μm) and thread designation (in).

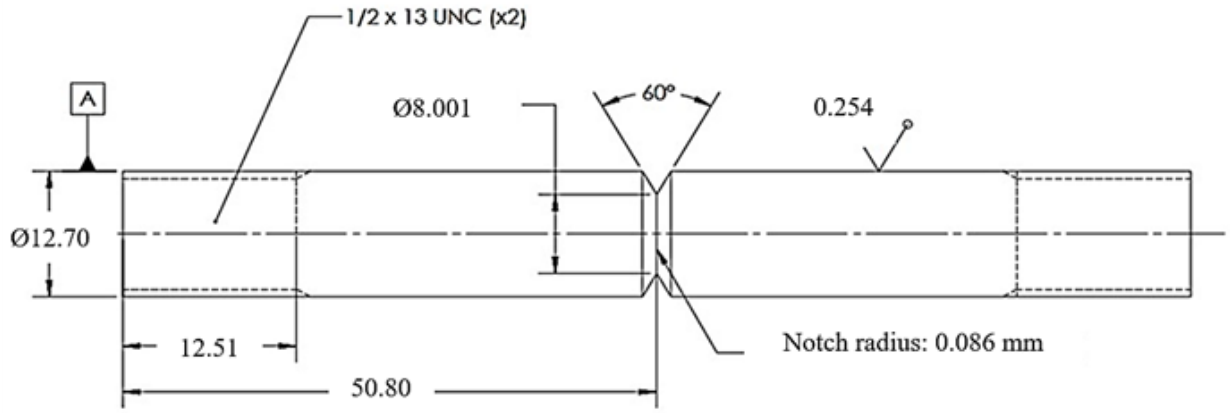

Figure 3.9: Drawing of 'large' circular notch tensile (CNT) specimen. Dimensions are in mm except for surface finish (μm) and thread designation (in).

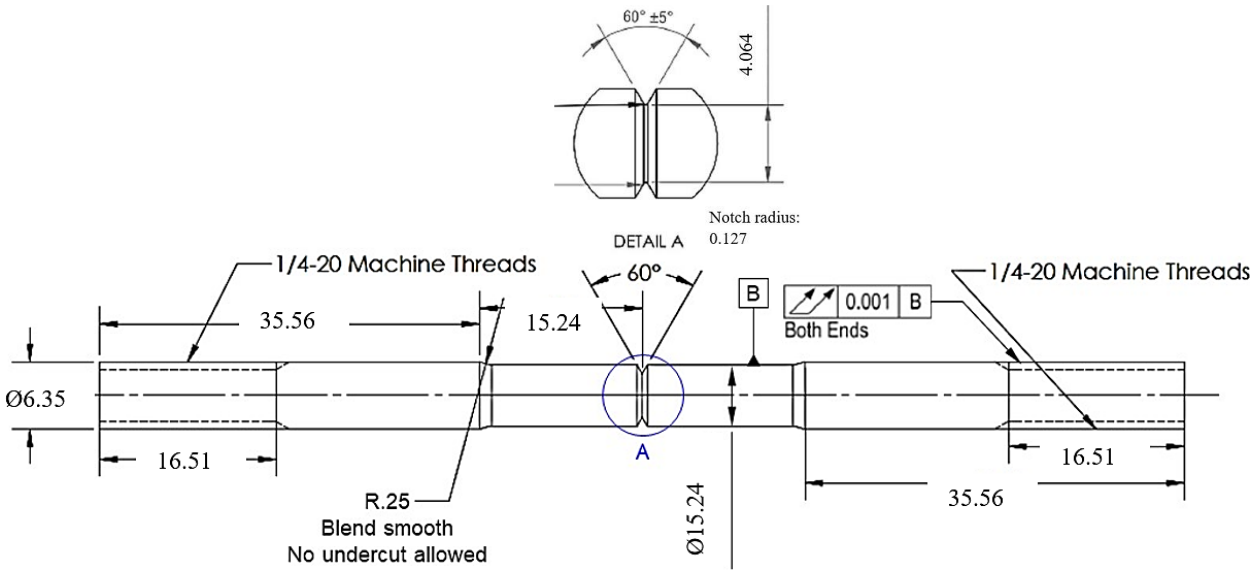

Figure 3.10: Drawing of ‘small’ circular notch tensile (CNT) specimen. Dimensions are in mm except for surface finish (μm) and thread designation (in).

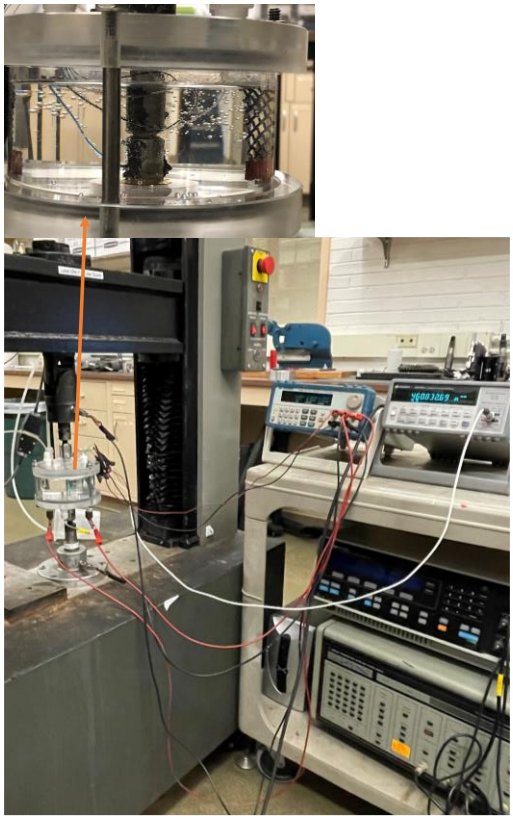

Figure 3.11: Hydrogen embrittlement experimental setup with the inset showing the CNT specimen in the acrylic chamber.

3.6. Fracture Surface Analysis

After the experiments, the fracture surface of the CNT specimens was cleaned with ethanol. Before further microscopic analysis, the fractured specimens were submerged in ethanol and put in an ultrasonic cleaner for 10 minutes. The fracture surface of all the CNT specimens was evaluated using a FEI QUANTA 600I® scanning electron microscope (SEM). The images were taken at the notch root, center, and overall fracture surface (low magnification) to observe the effects of hydrogen.

CHAPTER 4: RESULTS AND DISCUSSSION

4.1. Characterization of As-Received Condition of Alloys

A light optical microscope image of the as-received microstructure of 316L stainless steel (SS) is shown in Figure 4.1. The microstructure shows twin like features (as indicated by the red arrow in Figure 4.1) and is interpreted to reflect a cold-worked condition. The grain size for 316L SS was 70 μm. Light optical microscope images of the as-received microstructure of H1 and H2 are shown in Figure 4.2. The grain morphology of H1 is elongated along the RD compared to H2, reflecting a difference in thermomechanical process history. The grain size for H1 and H2 was 32 and 15 μm, respectively. Figure 4.3 shows XRD results for the as-received H1 and H2 alloys. In both alloys, the XRD peaks indicate that the microstructure is fully austenitic.

A light optical microscope image of the as-hot rolled microstructure of the V-microalloyed high Mn steel is shown in Figure 4.4. Microstructural and chemical banding can be observed in the as-hot rolled microstructure. The grain size was 30 μm for the as-hot rolled microstructure. Figure 4.5 shows the XRD results of the as-hot rolled V-microalloyed high Mn steel. The XRD results indicate a fully austenitic microstructure in all three conditions. VC precipitates were likely present at 600 and 650 °C aged conditions considering that the hardening was noted after aging, as will be discussed in section 4.2

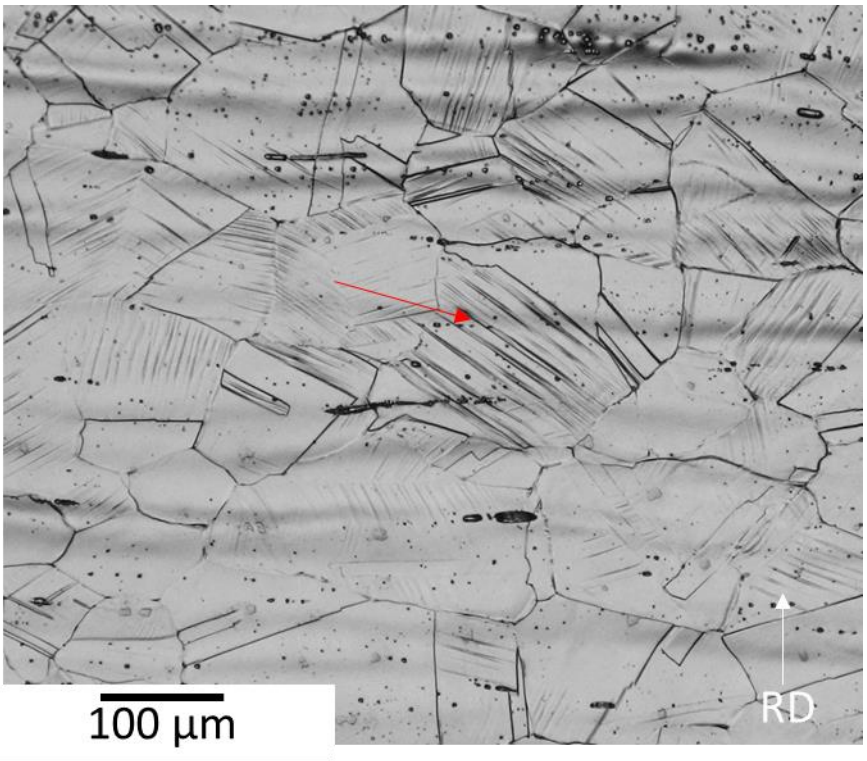

Figure 4.1: Light optical micrograph of the as-received microstructure of the 316L SS (Fe-0.017C-1.25Mn-17.57Cr-12.97Ni-0.03Nb-0.002Ti-0.59Ni-0.048N, all in wt pct). The white arrow indicates the rolling direction. The red arrow indicates twin like features (or stacking faults).

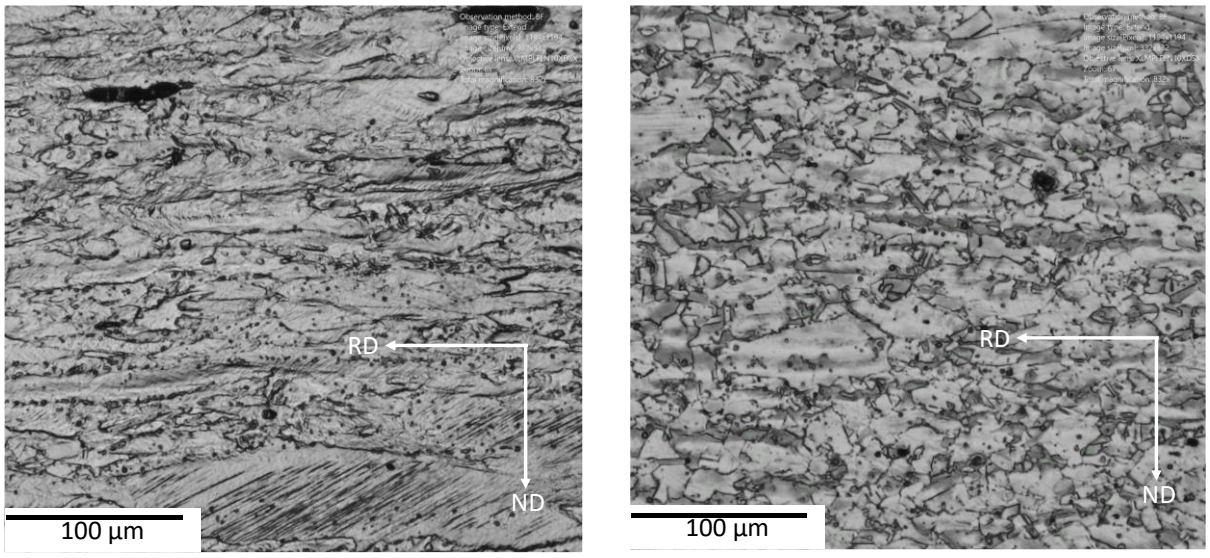

(a) (b)

Figure 4.2: Light optical micrographs of the as-received microstructures of high Mn alloys: (a) H1 (Fe-0.24C-30.0Mn-2.73Cr, all in wt pct) and (b) H2 (Fe-0.25C-30.4Mn-2.71Cr-3.0Ni-1.75Al all in wt pct).

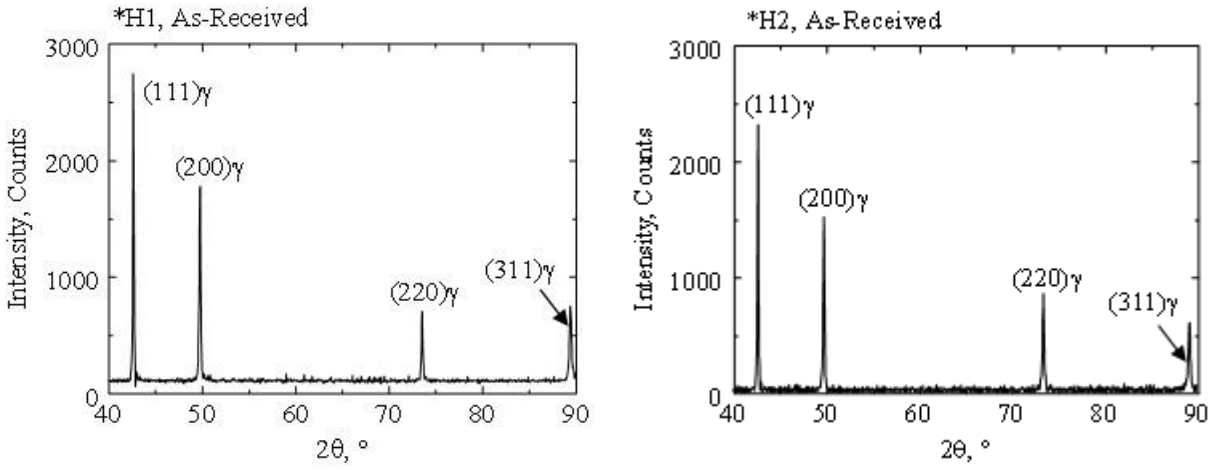

(a) (b)

Figure 4.3: XRD patterns (intensity versus 2θ°) of high Mn alloys in the as-received condition: (a) H1 (Fe-0.24C-30.0Mn-2.73Cr, all in wt pct) and (b) H2 (Fe-0.25C-30.4Mn-2.71Cr-3.0Ni-1.75Al all in wt pct).

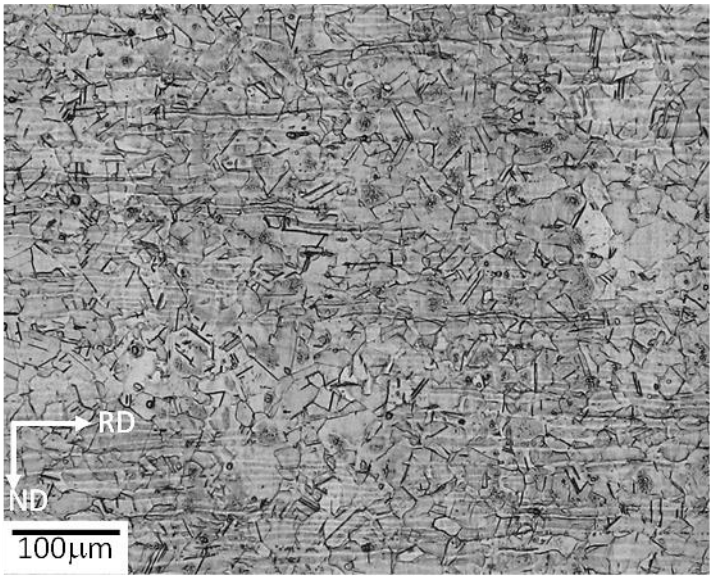

Figure 4.4: Light optical micrograph of the as-hot rolled (as-received) microstructure of the V-microalloyed high Mn alloy (Fe-0.262C-29.6Mn-1.66Al-2.87Ni-0.243V, all in wt pct).

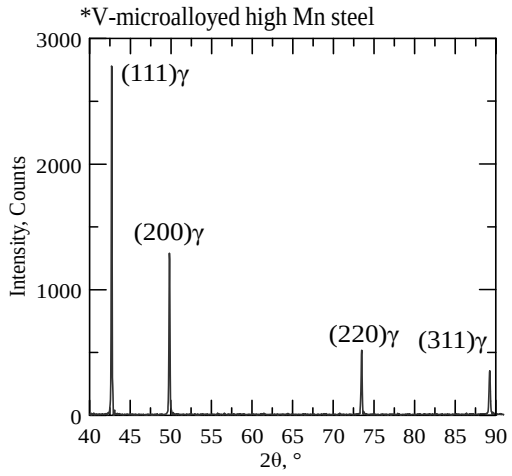

Figure 4.5: XRD data for the as-hot rolled, V-microalloyed high Mn austenitic alloy.

4.2. Cold Working and Heat Treatment Study

The hardness results for the V-microalloyed high Mn steel as a function of heat treatment conditions are shown in Figure 4.6. The hardness results from different grades of high Mn alloys (H1 and H2) and 316L SS are indicated in the figure for comparison. The hardness of 316L SS is higher than H1, H2, and all the V-microalloyed high Mn steel conditions. The 316L SS was cold-worked, which explains the high hardness value. The difference in hardness between H1 and H2 was not significant. There is an increase in the hardness of the V-microalloyed high Mn steel specimens aged at 600 and 650 °C for 1 hour compared to other heat treatment conditions, likely indicating the formation of vanadium carbide (VC) precipitates. The hardness values from temperatures ranging from 300 to 550 °C were lower compared to the non-aged as-received condition, which might be due to the competition between recovery and precipitate strengthening during aging. It is also possible that VC precipitation was not significant until higher temperatures of 600 or 650 °C.

Cold working to achieve 20 or 30 pct. cold working (CW) was performed on the V-microalloyed high Mn steel. The response to aging in conjunction with cold working of V-microalloyed high Mn steel was also analyzed. Figure 4.7 shows the average hardness values of cold worked V-microalloyed high Mn steel for various aging heat treatments. The hardness

values of the 20 and 30 pct. cold worked specimens were higher than all the conditions only subject to aging shown in Figure 4.6. Aging was performed on the 20-pct. cold worked specimens. It can be seen that 20-pct. cold worked specimens aged at 600 and 650 °C had higher hardness values than the non-aged, 20-pct. cold work condition. The 20-pct. cold worked condition showed more pronounced age-hardening compared to the hot rolled (i.e. non-cold rolled) V-microalloyed high Mn steel. The more prominent aging response may be attributed to finer VC precipitates or a higher volume fraction of precipitates for the cold worked conditions. An increase in dislocation density due to cold-working might increase the number of nucleation sites for VC compared to the hot rolled condition. Table 4.1 shows hardness values of high Mn alloys (H1 and H2), 316L SS, and all conditions of V-microalloyed High Mn steel.Light optical microscope images of the microstructures of the V-microalloyed high Mn steel after 20-pct. cold working and 20-pct. cold working with aging at 650 °C for 1 h are shown in Figure 4.8 (a) and (b). The grain size of the 20-pct. cold worked + aged condition was 25 µm when estimated according to ASTM E112 [105]. Figure 4.9 (a) and (b) show the XRD results of the samples after 20-pct. cold working and 20-pct. cold working in conjunction with aging (650 °C for 1h), indicating a fully austenitic matrix for both conditions.

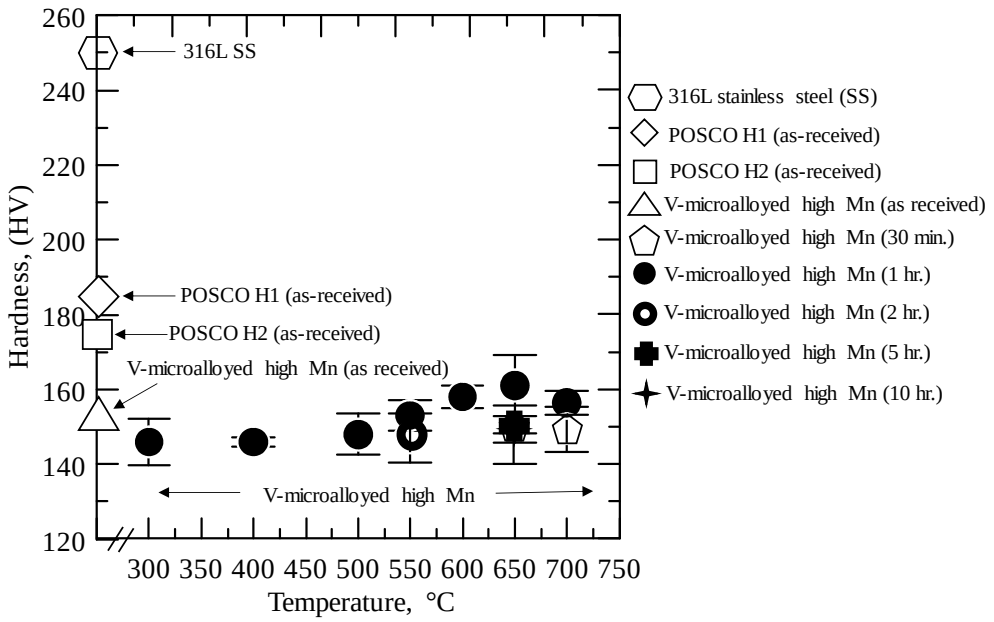

Figure 4.6: Average Vickers hardness values of the V-microalloyed high Mn steel as a function of aging time and temperature. The hardness results for the 316L SS, H1 and H2 high Mn alloys in the as-received condition are also shown. Error bars indicate standard deviation.

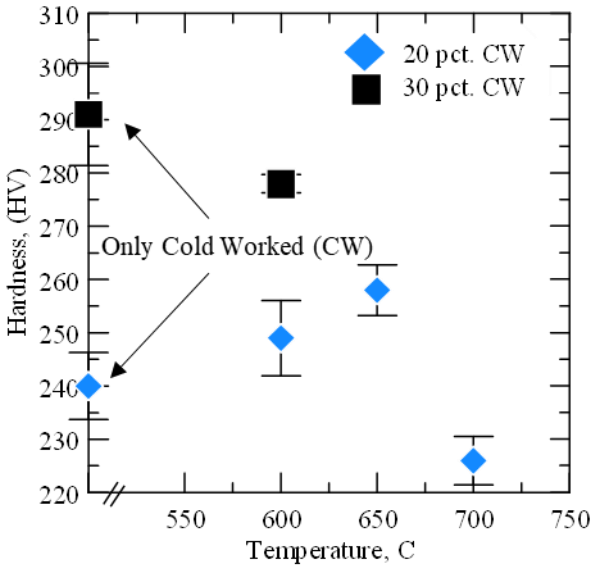

Figure 4.7: Average Vickers hardness values of the cold worked (CW) only and cold worked in conjunction with aging (duration - 1 hour) V-microalloyed high Mn steel as a function of temperature. Error bars indicate standard deviation.

Table 4.1: Hardness Values of High Mn Alloys (H1 and H2), 316L Stainless Steel (SS), and All Conditions of V-microalloyed High Mn Steel

Alloy	Conditions	Hardness (HV)
H1	As received	186±6.77
H2	As received	179±7.98
316L SS	As received	251±8.86
V-microalloyed high Mn steel	As received	153±3.70
V-microalloyed high Mn steel	Aged at 300 °C for 1hr.	146±6.14
V-microalloyed high Mn steel	Aged at 400 °C for 1hr.	146±1.30
V-microalloyed high Mn steel	Aged at 500 °C for 1hr.	148±5.41
V-microalloyed high Mn steel	Aged at 550 °C for 1hr.	153±4.05
V-microalloyed high Mn steel	Aged at 600 °C for 1hr.	158±3.14
V-microalloyed high Mn steel	Aged at 650 °C for 1hr.	161±8.30
V-microalloyed high Mn steel	Aged at 700 °C for 1hr.	156±3.20

Table 4.1: Continued

V-microalloyed high Mn steel	Aged at 550 °C for 2 hr.	147±6.74
V-microalloyed high Mn steel	Aged at 650 °C for 5 hr.	147±1.41
V-microalloyed high Mn steel	Aged at 650 °C for 10 hr.	147±3.74
V-microalloyed high Mn steel	Aged at 700 °C for 30 min.	149±6.02
V-microalloyed high Mn steel	20-pct. cold worked	240±6.26
V-microalloyed high Mn steel	30 pct. cold worked	291±9.62
V-microalloyed high Mn steel	20-pct. cold worked with aged at 600 °C for 1 hr.	249±7.07
V-microalloyed high Mn steel	20-pct. cold worked with aged at 650 °C for 1 hr.	258±4.74
V-microalloyed high Mn steel	20-pct. cold worked with aged at 700 °C for 1 hr.	226±4.57
V-microalloyed high Mn steel	30 pct. cold worked with aged at 600 °C for 1 hr.	278±1.70

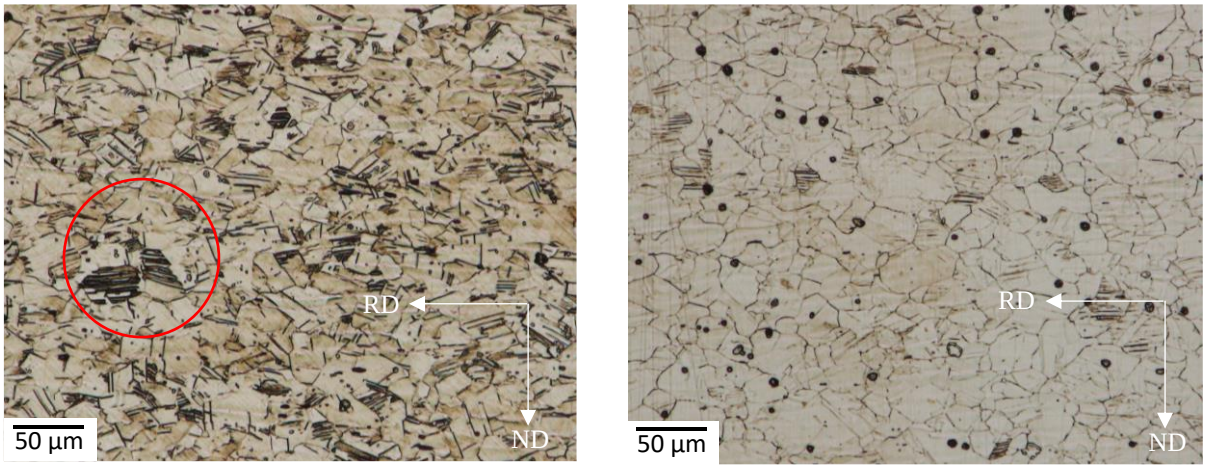

(a) (b)

Figure 4.8: Light optical micrographs of post processed microstructures of V-microalloyed high Mn alloy. (a) 20-pct. cold worked condition. (b) 20-pct. cold rolled and aged (650 °C-1 h) condition.

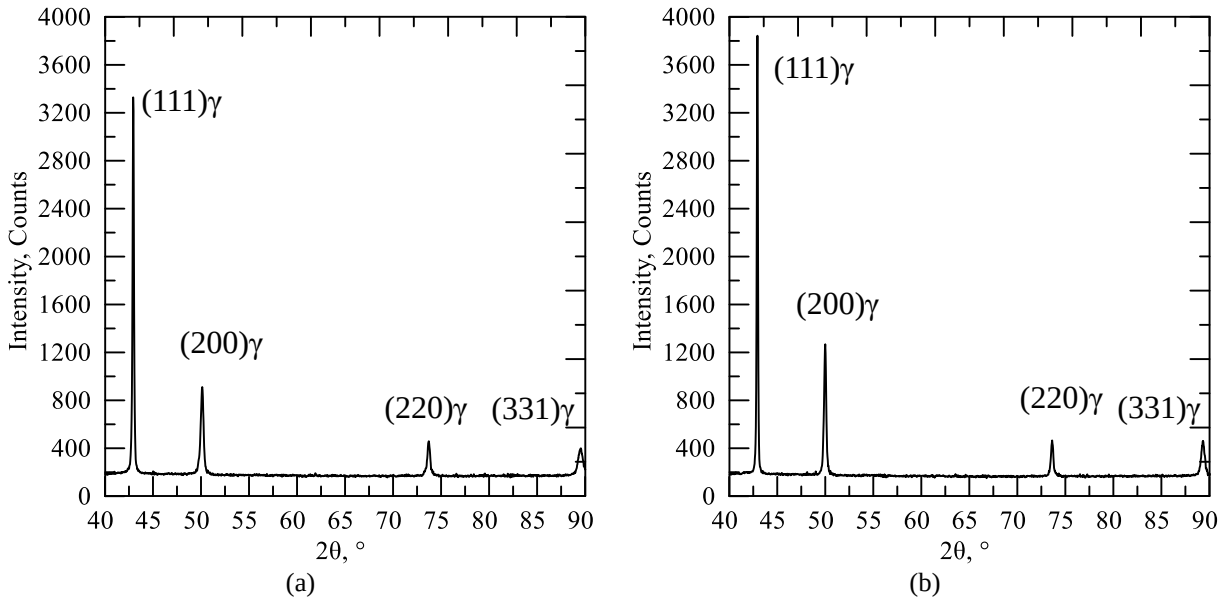

Figure 4.9: XRD patterns (intensity versus 2θ°) of V-microalloyed high Mn austenitic (γ) steel in the (a) 20 pct cold rolled condition and (b) 20-pct. cold rolled and aged (650 °C-1h) condition.

4.3. Tensile Properties

In this study, a yield strength level between 400 and 800 MPa was targeted for the designed alloy to accommodate strength requirements for various hydrogen applications. Table 4.2 presents the tensile properties of 316L SS, H1, H2, and all conditions of the V-microalloyed high Mn steel. The ultimate tensile strengths of high Mn alloys (H1 and H2) are higher than 316L SS, but the hardness of the high Mn alloys is lower than that of 316L SS (see Figure 4.6). Further analysis should be performed for this anomaly. The engineering stress-strain curves of 316L SS, H1 and H2 can be seen in Figure 4.10. The yield strength of 316L SS is higher than both H1 and H2; note that the bar material of the 316L SS was received in a cold-worked condition. The ductility of H1 is higher than the 316L SS, H2 alloy, and post processed conditions of V-microalloyed high Mn steel but less than the hot rolled V-microalloyed high Mn steel condition. As discussed in Section 4.5, deformation twinning is more prominent in H1 compared to H2 and V-microalloyed high Mn steel due to the lower SFE of H1 (28.9 $mJ \cdot m^{-2}$).The engineering stress-strain curves of 316L SS and as-hot rolled, 20-pct. cold work only, and 20-pct. cold work in conjunction with aging (650 °C for 1h) conditions of the V-microalloyed high Mn Steel are shown in Figure 4.11. The as-hot rolled V-microalloyed high Mn condition has lower yield strength but higher ductility than the 316L SS, H1, and H2 conditions. The lower

strength and higher ductility were partly the basis for applying cold working for strength enhancement in this alloy.

The 20-pct. cold worked condition of the V-microalloyed high Mn steel has a higher yield and ultimate tensile strength than the as-hot rolled condition and the 316L SS, as shown in Figure 4.11. It has lower ductility compared to the hot rolled condition. The 20 pct. cold worked in conjunction with aging (650 °C for 1h) condition has higher ultimate strength and lower yield strength compared to the 316L SS. It has a higher ductility compared to the 20 pct. cold worked only condition. The lower strength of the cold worked and aged condition implies that the aging decreases the dislocation density, and strength loss due to recovery was not compensated by precipitate strengthening. It should be noted that all post-processed V-microalloyed high Mn steel conditions have a comparable total elongation to that of 316L SS. The 20 pct cold worked and 20-pct. cold worked with aging conditions of the V-microalloyed high Mn steel have higher strength than the H1 and H2 alloys. The 20-pct. cold worked condition of V-microalloyed high Mn steel is close to the upper limit (800 MPa) of the target yield strength.

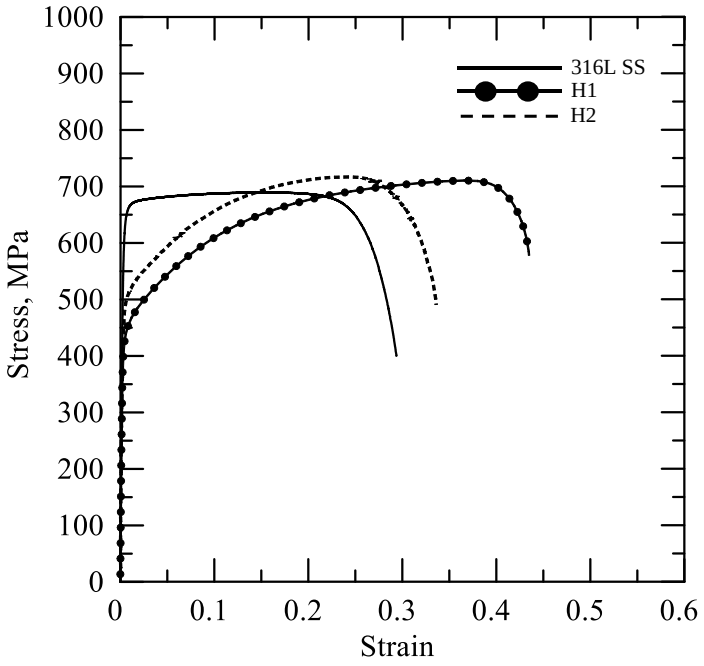

Figure 4.10: Engineering stress versus engineering strain plots for the as-received 316L SS, H1 and H2 alloys.

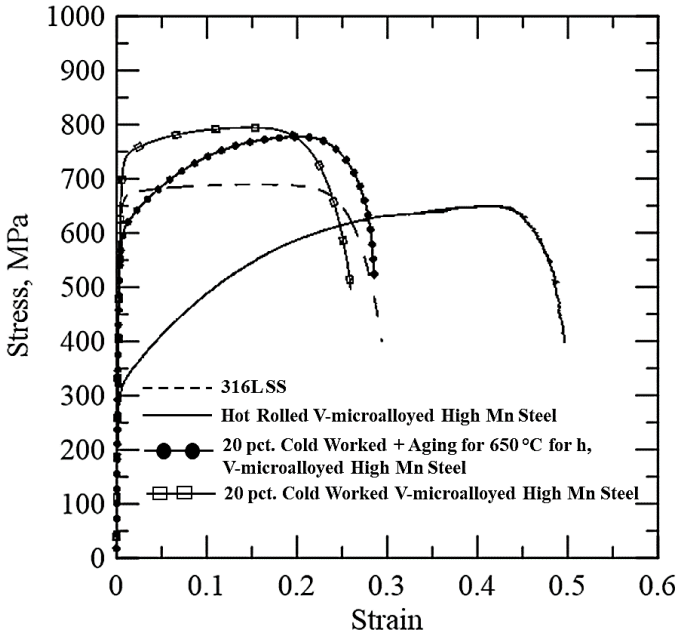

Figure 4.11: Engineering stress versus engineering strain curves for 316L SS and 20-pct. cold work only and 20-pct. cold work in conjunction with aging (650 °C-1h) conditions of V-microalloyed high Mn steel.

Table 4.2: Tensile Properties of High Mn Alloys (H1 and H2), 316L Stainless Steel (SS) and V-microalloyed High Mn Steel in Different Conditions

Alloy	Yield Strength (MPa)	Ultimate Tensile Strength (MPa)	Uniform Elongation (pct.)	Total Elongation (pct.)
H1	439	710	37.0	43.0
H2	485	717	25.0	34.0
316L SS	641	690	16.0	30.0
Hot rolled V-microalloyed high Mn steel	310	649	40.0	49.0
20-pct. cold worked V-microalloyed high Mn steel	716	794	14.0	26.0
20-pct. cold worked + aging for 650 °C at 1h V-microalloyed high Mn steel	587	777	19.0	29.0

4.4. Hydrogen Embrittlement Results

Table 4.3 lists the notch tensile strength (NTS), ratio of NTS in hydrogen and air (closer to one indicates high hydrogen embrittlement resistance), and specimen geometry used for the high Mn alloys (H1 and H2), 316L SS, and V-microalloyed high Mn steel, obtained from rising displacement testing in the hydrogen-charged condition and air.

The stress versus displacement behavior for the CNT specimens of 316L SS tested in the electrochemical hydrogen environment (0.05 M NaOH aqueous solution – current density of 1.65 $mA \cdot cm^{-2}$) and air are shown in Figure 4.12. There is no indication of a hydrogen embrittlement effect on the notch tensile properties of 316L SS, i.e. the NTS for the hydrogen-charged specimen was higher than for the specimen tested in air. These results are consistent with a technical report published by Sandia National Laboratories [107]. They tested notch tensile specimens of 316 SS in a 70 MPa gaseous hydrogen environment at room temperature and found no strength degradation in the hydrogen environment compared to air. Figure 4.13 shows an SEM fractograph taken near the notch root of the 316L SS CNT specimen in the hydrogen-charged condition. The fracture surface shows microvoid coalescence (ductile features), which further validates its high hydrogen resistance; 316L SS is commonly used for hydrogen storage and transportation applications because of its established resistance to hydrogen embrittlement.

The stress versus displacement behavior for the H1 and H2 CNT specimens tested in the hydrogen environment (0.05 M NaOH aqueous solution – current density of 1.65 $mA \cdot cm^{-2}$) and air are shown in Figure 4.14. There is no significant NTS degradation of the H2 alloy in the hydrogen-charged condition compared to the air condition. However, the H1 alloy exhibited a lower NTS in the hydrogen-charged condition compared with air condition, indicating a hydrogen embrittlement effect. Figure 4.15 shows SEM fractographs taken near the notch root of the H1 and H2 alloys. The H1 alloy exhibits transgranular brittle fracture, which is indicative of hydrogen embrittlement. The H2 alloy displays microvoid coalescence, which is consistent with its insignificant NTS degradation.

The stress versus displacement behavior of the as-hot rolled, 20- pct cold worked and 20-pct. cold worked with aging (650 °C for 1h) conditions for V-microalloyed high Mn steel tested in the hydrogen environment (0.05 M NaOH aqueous solution – current density of 1.65 $mA \cdot cm^{-2}$) and air are shown in Figure 4.16. The CNT geometry for the 20-pct. cold worked and 20 pct.

cold worked with aging (650 °C for 1h) conditions of V-microalloyed high Mn steel was modified due to the reduced thickness of base plates after cold working. According to Kong *et al.* [106], similar specimen geometry differences for 255 duplex stainless steel specimens tested under comparable environments have little effect on the measured NTS.

The hot rolled condition had significant NTS degradation in the hydrogen-charged condition versus air. Figure 4.17 shows an SEM fractograph taken near the notch root of the hot rolled condition in the hydrogen-charged condition. The fractograph shows intergranular brittle fracture in addition to transgranular cleavage fracture, which is consistent with hydrogen embrittlement. The 20-pct. cold worked condition had a minor decrease in NTS degradation in hydrogen-charged condition versus air as shown in Figure 4.16. Figure 4.18 shows an SEM fractograph taken near the notch root of the 20-pct. cold worked condition in the hydrogen-charged condition. The 20 pct cold worked condition shows both intergranular and transgranular fracture, which is a feature of hydrogen embrittlement. However, the 20-pct. cold worked with aging (650 °C for 1h) condition demonstrated no NTS degradation in the hydrogen-charged condition versus air as shown in Figure 4.16. Figure 4.19 shows an SEM fractograph of the 20-pct. cold work in conjunction with aging (650 °C for 1h) condition of the V-microalloyed high Mn steel in the hydrogen-charged condition. The image shows microvoid coalescence near the notch root, which is consistent with its higher hydrogen embrittlement resistance. The 20-pct. cold worked with aging (650 °C for 1h) condition had comparable hydrogen performance (NTS and fracture surface in the hydrogen-charged condition) to that of 316L SS.

Table 4.3: Notch Tensile Strength of High Mn Alloys (H1 and H2), 316L Stainless Steel (SS), and V-microalloyed High Mn Steel in Different Conditions in the Hydrogen-charged Condition and Air.

Alloy	Notch Tensile Strength in Air (MPa)	Notch Tensile Strength in Hydrogen Charging Environment (MPa)	Performance Ratio (Hydrogen/Air)	CNT Specimen Geometry
H1	854	755	0.89	'Large'
H2	893	843	0.94	'Large'
316L SS	1150	1180	1.02	'Large'
As-hot rolled V-microalloyed high Mn steel	805	663	0.83	'Large'
20-pct. cold worked V-microalloyed high Mn steel*	1274	1222	0.95	'Small'
20-pct. cold worked + aged (650 °C-1 h) V-microalloyed high Mn steel	1086	1086	1.0	'Small'

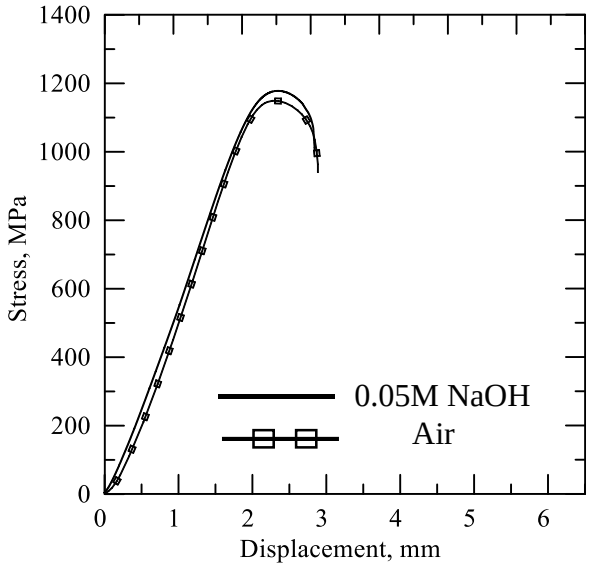

Figure 4.12: Stress as a function of displacement for representative circular notched tensile (CNT) specimens of 316L SS obtained from rising displacement testing in an electrochemical hydrogen charging environment (0.05 M NaOH aqueous solution and current density of 1.65 $mA \cdot cm^{-2}$) and air.

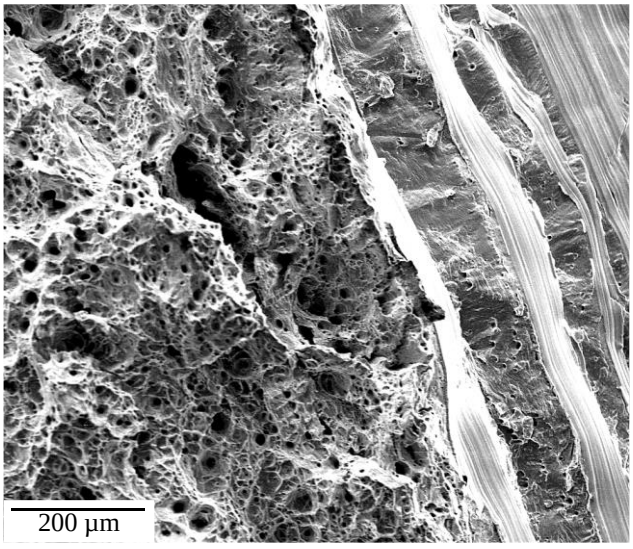

Figure 4.13: SEM fractograph of the 316L SS CNT specimen tested in the electrochemical charging environment using a 0.05M NaOH aqueous solution. The SEM image was taken near the notch root.

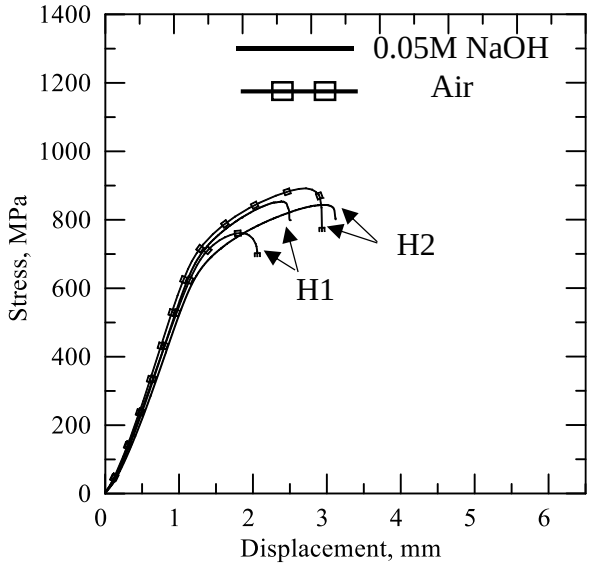

Figure 4.14: Stress as a function of displacement for H1 and H2 CNT specimens obtained from rising displacement testing in a hydrogen charging environment and air.

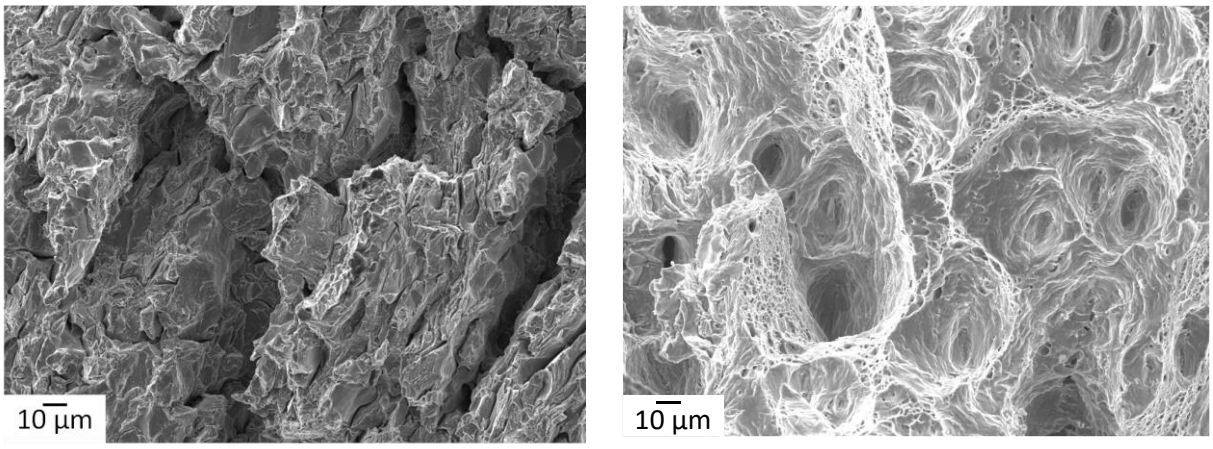

(a) (b)

Figure 4.15: SEM fractographs of the CNT specimens tested in the electrochemical charging environment using a 0.05M NaOH aqueous solution. The SEM images were taken near the notch root of the (a) H1 and (b) H2 alloy specimens.

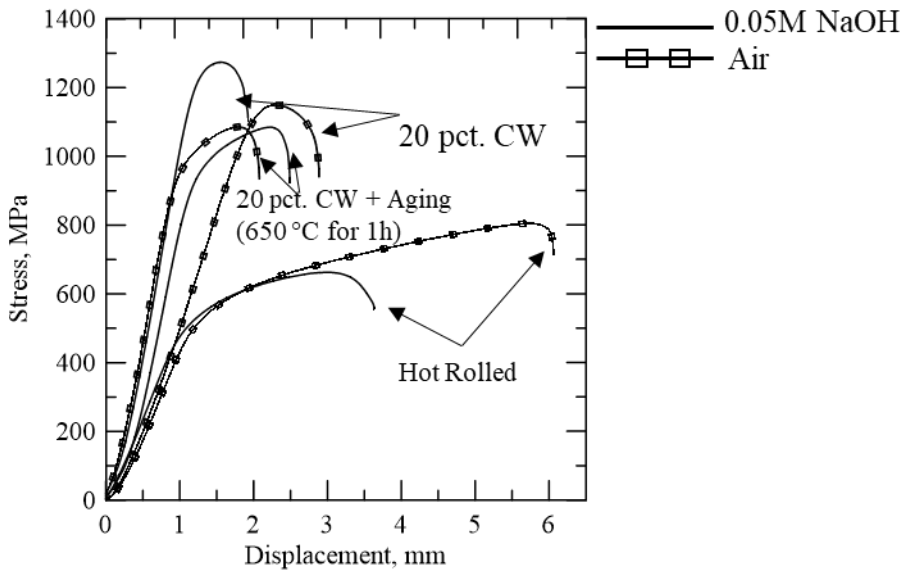

Figure 4.16: Stress as a function of displacement for CNT specimens of the as-hot rolled, 20-pct cold worked (CW), and 20-pct CW + aged (650 °C-1 h) conditions, obtained from rising displacement testing in a 0.05M NaOH aqueous solution hydrogen charging environment and air. Note that the results for the as-hot rolled condition were obtained using *large* CNT specimens, whereas the *small* CNT specimen geometry was used for 20-pct. cold worked and 20-pct. cold worked with aging post processed condition.

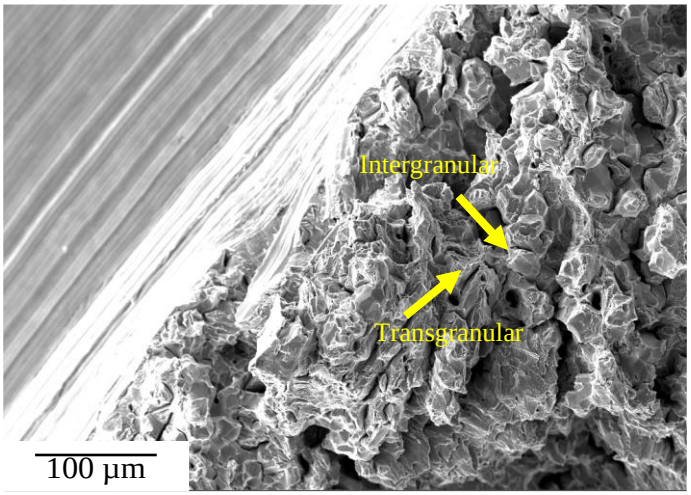

Figure 4.17: SEM fractograph of the as-hot rolled V-microalloyed high Mn steel CNT specimen tested in the electrochemical charging environment using a 0.05M NaOH aqueous solution, taken near the notch root.

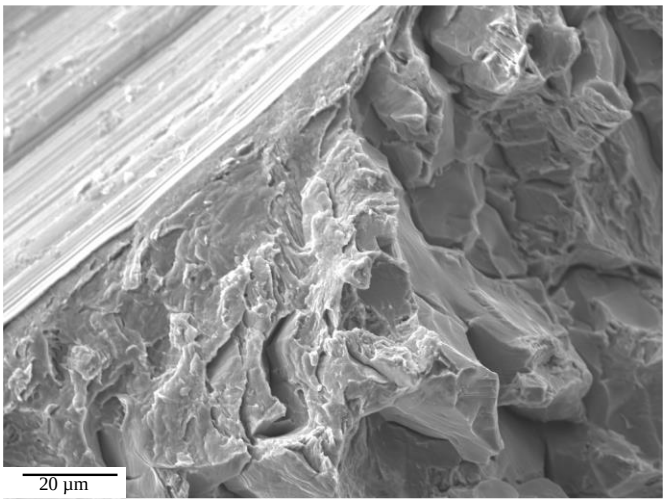

Figure 4.18: SEM fractograph of the 20-pct. cold worked only condition of the V-microalloyed high Mn steel CNT specimen tested in the electrochemical charging environment using a 0.05M NaOH aqueous solution taken near the notch root.

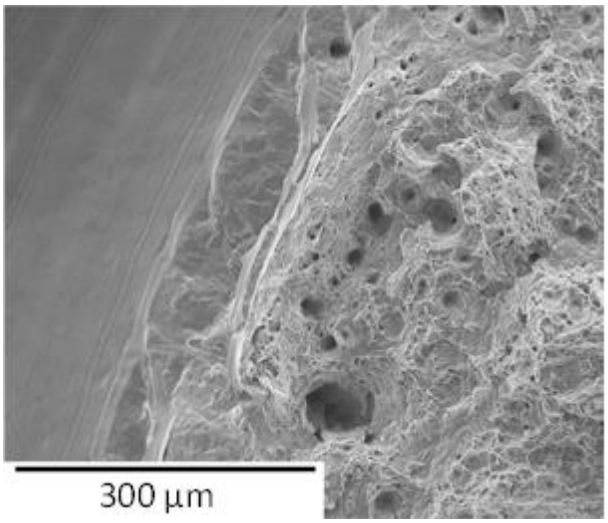

Figure 4.19: SEM fractograph of the 20-pct. cold worked + aged (650 °C for 1h) condition of the V-microalloyed high Mn steel CNT specimen tested in the electrochemical charging environment using a 0.05M NaOH aqueous solution taken near the notch root.

4.5. Characterization of Deformed High Mn Alloys

The phase stability of austenite plays an integral part in having a high hydrogen embrittlement resistance. Figure 4.20 shows the XRD patterns of deformed tensile specimens of the H1 and H2 conditions. The specimens for the XRD analysis were taken from the fractured tensile specimens near the fracture surface. After deformation, the H1 alloy exhibited low intensity peaks associated with ε-martensite in addition to more intense austenite peaks. The martensite peaks imply the formation of strain-induced martensite. Strain-induced martensite is more vulnerable to hydrogen embrittlement than austenite [113], which explains the poor hydrogen performance of the H1 alloy. Figure 4.21 shows EBSD results for the deformed H1 microstructure with image quality, inverse pole figure, and phase maps. The inverse pole figure map indicates deformation twinning. While the phase map indicates mostly austenite in deformed H1; a small fraction of ε martensite was also detected by EBSD as indicated by the yellow color in Figure 4.21. Note that the phase map in Figure 4.21 shows data with confidence indices greater than 0.1 and specifically, the region of ε martensite had confidence indices much greater than 0.1. The planar slip deformation mechanisms are consistent with the calculated SFE of 28.9 $mJ \cdot m^{-2}$ of the H1 alloy. As discussed in Chapter 2, deformation mechanisms of austenitic alloys depend on SFE. It has been empirically shown that deformation twinning becomes prominent at an intermediate range of SFE ($15\ mJ \cdot m^{-2} < SFE < 45\ mJ \cdot m^{-2}$) [111].

After tensile deformation, the H2 alloy exhibited austenitic peaks only (Figure 4.20 (b)), which validates its high austenite phase stability against martensitic transformation. Figure 4.22 shows the EBSD results for the deformed H2 microstructure with image quality, inverse pole figure, and phase maps. The inverse pole figure map indicates a smaller fraction of deformation twins compared to the H1 alloy. The phase map of H2 indicates only austenite which is consistent with its high SFE of 49 $mJ \cdot m^{-2}$; a high SFE promotes a dislocation glide-dominant deformation mechanism, which positively contributes to hydrogen embrittlement resistance [53].

Figure 4.23 shows the XRD pattern from a deformed tensile specimen of the hot rolled V-microalloyed high Mn steel, which was taken from the fractured tensile specimen near the fracture. The XRD results indicate low-intensity peaks associated with ε-martensite and more intense austenite peaks. Figure 4.24 shows EBSD results of the deformed microstructure of the hot rolled V-microalloyed high Mn steel, with image quality, inverse pole figure, and phase maps. The phase map shows mostly austenite in the deformed state indicated in Figure 4.24.

Martensite observed from the XRD result is likely associated with the lower hydrogen embrittlement resistance of the V-microalloyed high Mn steel in the as-hot rolled condition compared to the H2 alloy. The volume fraction of deformation twins in hot rolled V-microalloyed high Mn steel is also higher compared to H2 but significantly less than the H1 alloy.

The relatively high hydrogen embrittlement susceptibility of the as-hot rolled V-microalloyed steel is *not* as expected considering its high SFE (the calculated SFE of hot rolled V-microalloyed high Mn steel is higher than H1 and comparable to H2). The characterization results indicated low austenitic stability, which increases hydrogen embrittlement susceptibility, as discussed in Chapter 2.

The grain size of the hot-rolled V-microalloyed steel (32 μm) is larger than that of H2 (15 μm) (observe Figures 4.2 and 4.4). Zan *et al.* [110] studied the effects of grain size on the hydrogen embrittlement performance of an Fe-22Mn-0.6C austenitic alloy using different processing route. The intergranular fracture was the primary indicator of hydrogen embrittlement. They measured the depth of intergranular (brittle) fracture from the surface. The specimen with a larger grain size had higher hydrogen embrittlement depth than the finer grain size specimen. They attributed poor hydrogen performance of coarser grained microstructure to diffusible hydrogen content. The hydrogen absorbed per unit grain boundary area is higher as the grain size increases.

Figure 4.25 shows light optical micrographs of the microstructure from the fractured CNT specimen, tested in air, of the 20-pct. cold worked with aging (650 °C for 1h) condition of the V-microalloyed high Mn steel. Figure 4.25 (a) and (b) show the microstructures of the undeformed and deformed regions, respectively. Both areas showed some features associated with deformation twins due to cold working. Figure 4.26 shows a light optical micrograph of the microstructure from the fractured CNT specimen of the 20-pct. cold worked with aging (650 °C for 1h) condition of the V-microalloyed high Mn steel taken from the deformed region after testing in the 0.05M NaOH solution while electrochemically charging the specimen with hydrogen. The deformed region may have a higher frequency of deformation twins (highlighted with a circle) formed near the fracture surface. Planar deformation mechanisms are typically associated with poor hydrogen embrittlment susceptibility. However, the hydrogen

embrittlement performance of 20-pct. Cold worked with aging (650 °C for 1h) condition was better than hot rolled condition of V-microalloyed high Mn steel, H1 and H2 alloy.

Michler *et al.* [114] proposed that the high dislocation density of cold worked austenitic alloys slows hydrogen diffusion, leading to the high hydrogen embrittlement resistance. The same mechanism might hold true for post processed conditions of V-microalloyed high Mn steel. Further analysis has to be done to explore the mechanism behind cold working and hydrogen embrittlement.

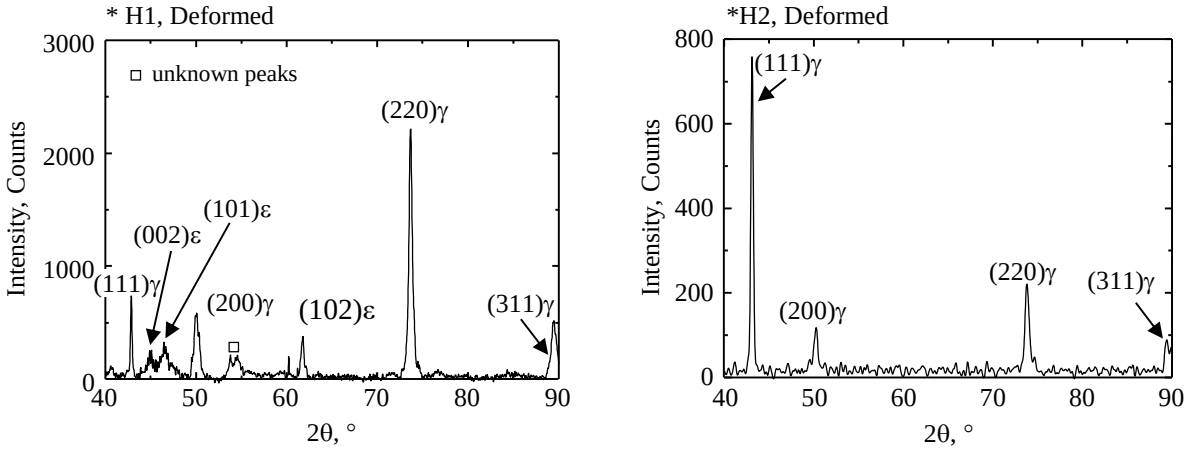

(a) (b)

Figure 4.20: XRD patterns (intensity versus 2θ) of high Mn alloys after tensile testing (deformation) in air. (a) H1 (Fe-0.24C-30.0Mn-2.73Cr, all in wt pct). (b) H2 (Fe-0.25C-30.4Mn-2.71Cr-3.0Ni-1.75Al all in wt pct).

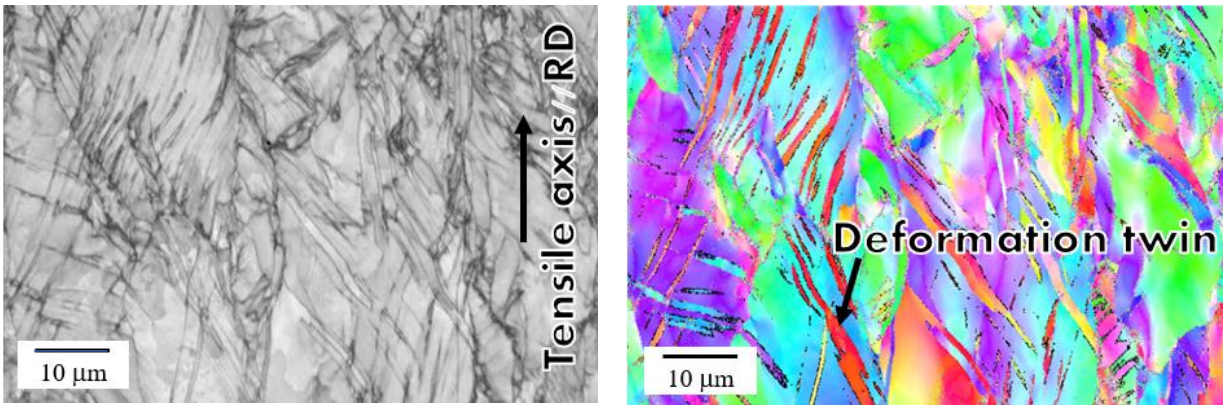

(a) (b)

Figure 4.21: EBSD results for the high Mn alloy H1 (Fe-0.24C-30.0Mn-2.73Cr, all in wt pct) alloy. (a) Image quality map. (b) Inverse pole figure map. (c) Phase map for austenite (red), ferrite or α′-martensite (green), and ε-martensite (yellow). In (b), black lines indicate Σ3 twin boundaries, mostly associated with deformation twins (*color images – See PDF version*).

Figure 4.21: Continued

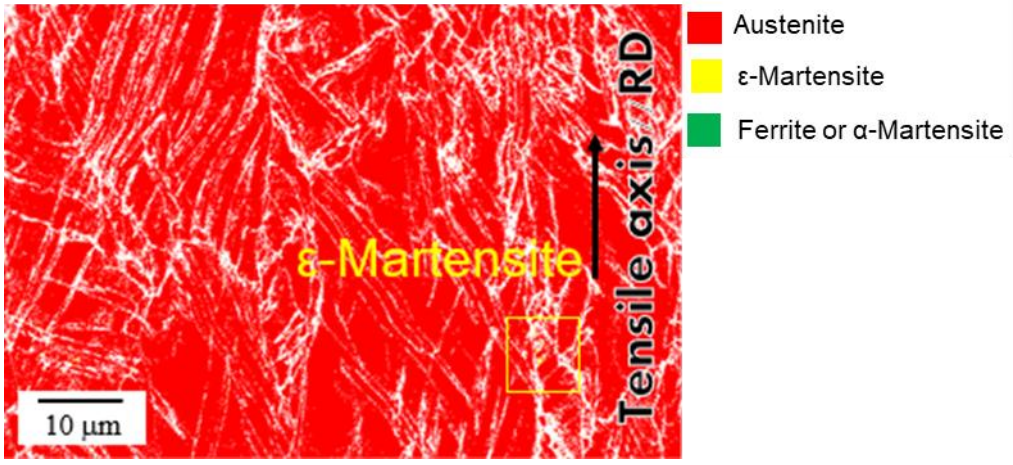

(c)

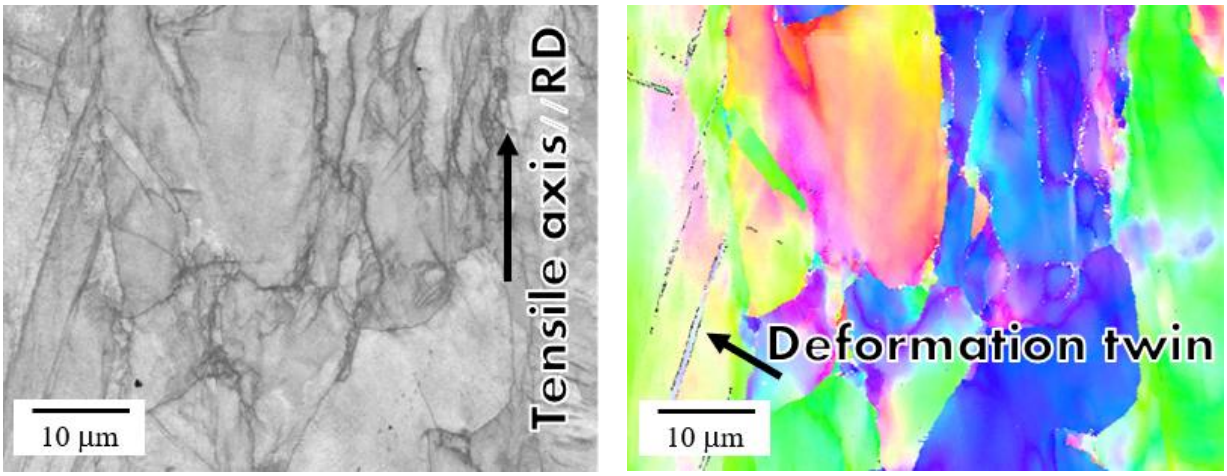

(a) (b)

Figure 4.22: EBSD results for the high Mn alloy H2 (Fe-0.25C-30.4Mn-2.71Cr-3.0Ni-1.75Al all in wt pct). (a) Image quality map. (b) Inverse pole figure map. (c) Phase map for austenite (red), ferrite or α′-martensite (green), and ε-martensite (yellow). In (b), black lines indicate Σ3 twin boundaries, mostly associated with deformation twins (*color images – See PDF version*).

Figure 4.22: Continued

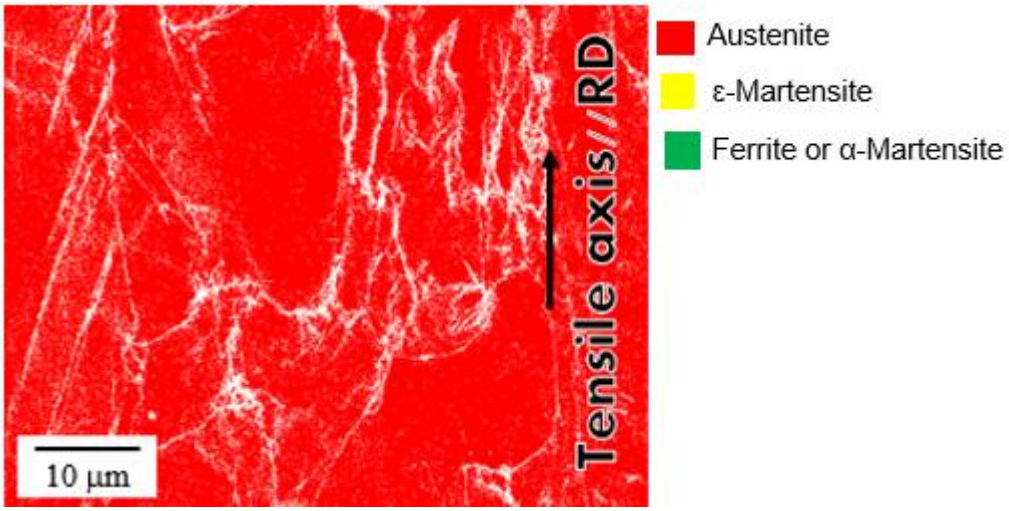

(c)

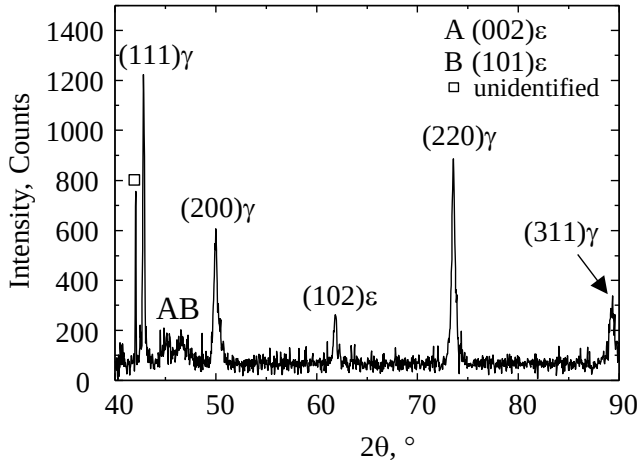

Figure 4.23: XRD pattern (intensity versus 2θ) of the hot rolled V-microalloyed high Mn steel after tensile testing (deformation) in air (Fe-0.262C-29.6Mn-2.87Ni-1.66Al-0.243, all in wt. pct.).

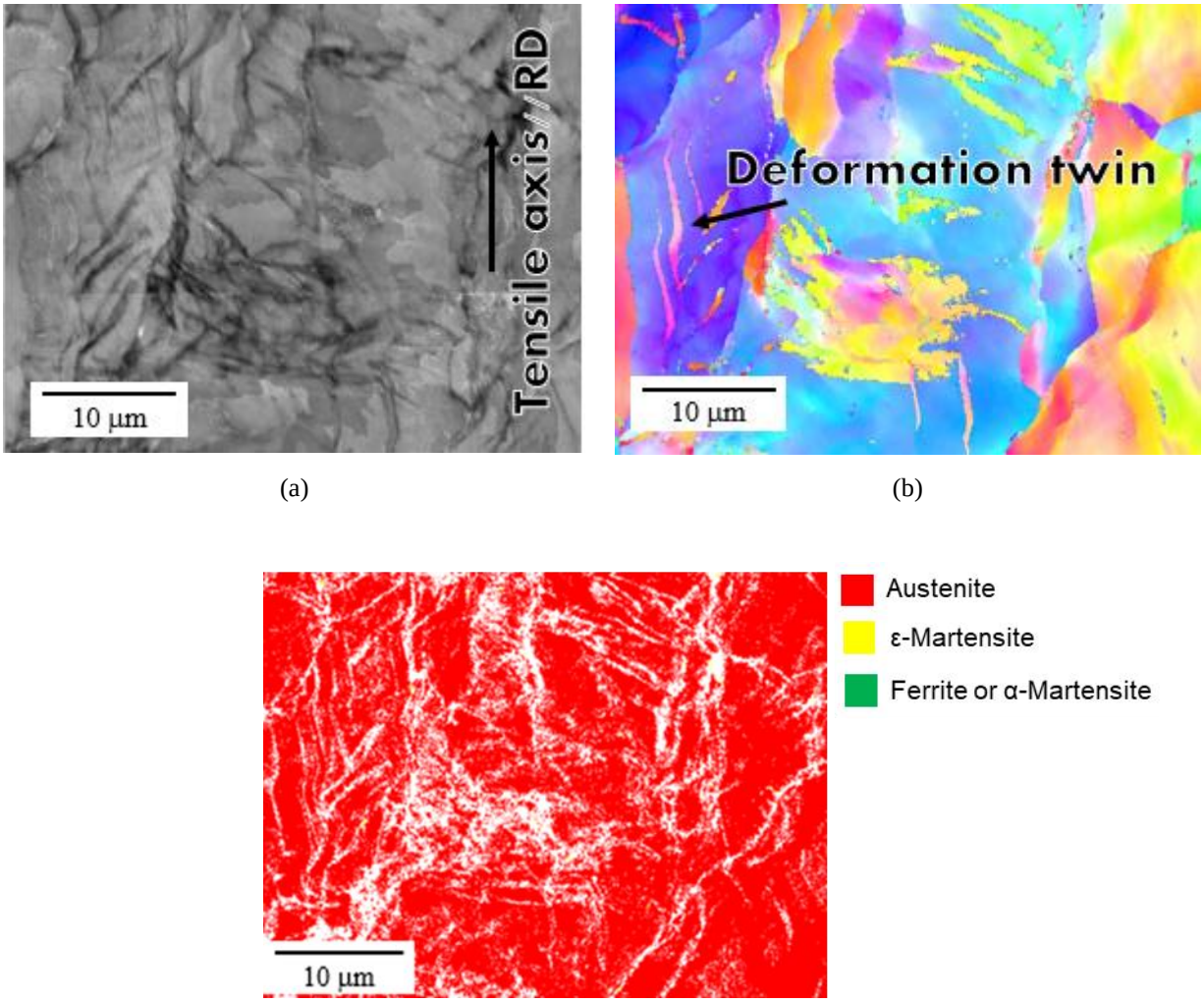

(a) (b)

(c)

Figure 4.24: EBSD results of the fractured tensile specimen of hot rolled V-microalloyed high Mn steel (Fe-0.262C-29.6Mn-2.87Ni-1.66Al-0.243, all in wt. pct.) (a) Image quality map. (b) Inverse pole figure map. (c) Phase map for austenite (red), ferrite or α′-martensite (green), and ε-martensite (yellow). In (b), black lines indicate Σ3 twin boundaries, mostly associated with deformation twins (*color images – See PDF version*).

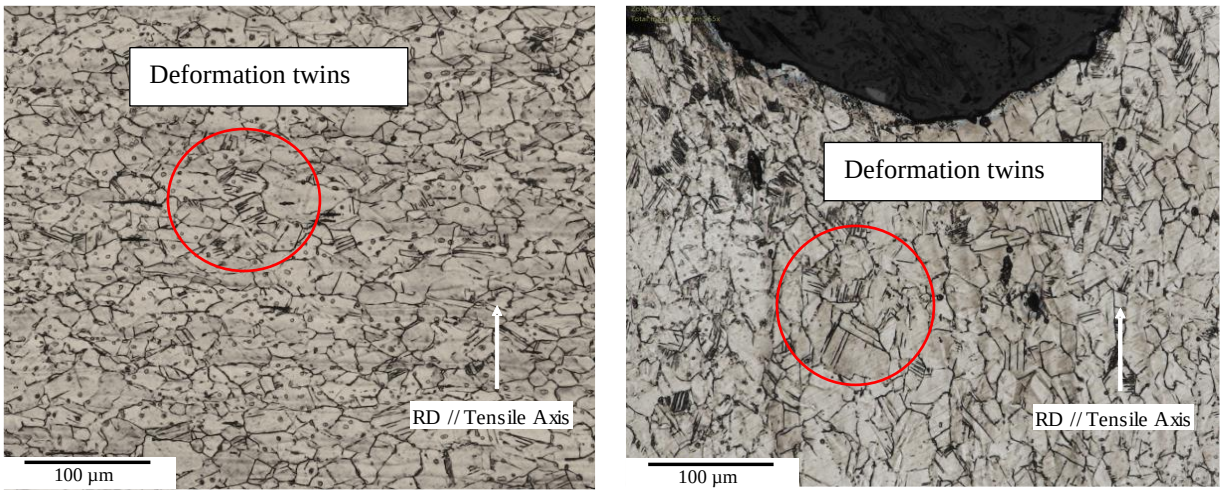

(a) (b)

Figure 4.25: Light optical micrographs of the microstructure in a fractured specimens from the (a) undeformed region and (b) deformed region of the 20-pct. cold worked with aging condition of the V-microalloyed high Mn steel specimen tested in the air environment.

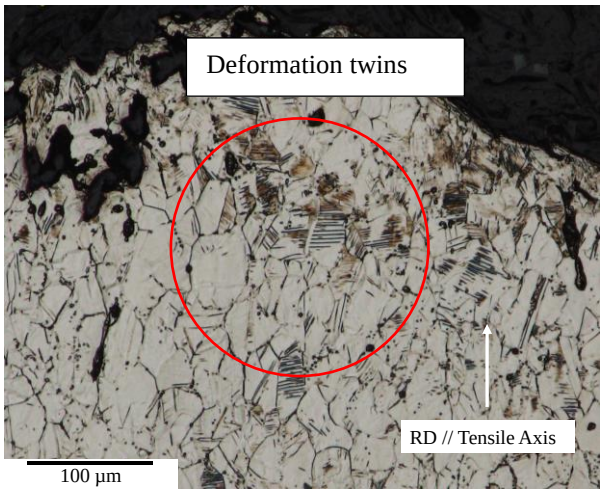

Figure 4.26: Light optical micrographs of the microstructure in a fractured specimens from the deformed region of the 20-pct. cold worked in conjunction with aging (650 °C for 1h) condition of the V-microalloyed high Mn steel specimen tested in the electrochemical hydrogen charging environment.

4.6. Summary

The designed V-microalloyed high Mn steel is compared against 316L SS, H1, and H2 alloys. The experiments proved that austenitic stability plays an integral role in hydrogen embrittlement resistance. Processing (hot rolling, 20-pct. cold working, and 20 pct cold working with aging) of the designed V-micro alloyed high Mn steel also influences the hydrogen embrittlement resistance. The 20 pct cold worked with the aging condition of V-microalloyed high Mn steel had a hydrogen embrittlement resistance comparable to 316L SS, whereas the 20 pct cold worked and hot rolled conditions had higher hydrogen embrittlement susceptibility. The

tensile strength properties of the 20-pct cold worked and 20-pct cold worked with aging conditions of V-microalloyed high Mn steel were within the targeted range.

CHAPTER 5: SUMMARY AND CONCLUSIONS

The objective of this project is to develop low-cost high Mn steels with high hydrogen embrittlement resistance. This project aimed to address the following research questions:

- Does stacking fault energy (SFE) calculated based on thermodynamic modeling predict the hydrogen performance for the high Mn alloys?
- How do post-processing parameters like cold working and aging affect the hydrogen performance of designed V-microalloyed high Mn steel?

The relative hydrogen embrittlement resistance for H1 and H2 alloys inferred from the calculated SFE agreed with the in situ rising displacement test results for circumferentially notched tensile specimens in a hydrogen charged environment (0.05 M NaOH aqueous solution - current density 1.65 $mA \cdot cm^{-2}$). The H1 alloy with the calculated SFE of 28.9 $mJ \cdot m^{-2}$ experienced degradation of notch tensile strength in the hydrogen environment. Transgranular brittle fracture features were present at the notch root of the fracture surface. The XRD and EBSD results of the deformed H1 alloy specimens indicated the presence of strain-induced ε-martensite in addition to austenite. The austenite phase stability and SFE play an influential role in hydrogen embrittlement resistance. SFE influences the deformation mechanisms; planar slip mechanisms such as deformation induced twinning and martensite formation promote hydrogen embrittlement for austenitic alloys, which corresponds to the deformation mechanisms and hydrogen embrittlement test results noted for H1 alloy. H2 alloy showed only a small loss of notch tensile strength in a hydrogen environment, and ductile features were present at the notch root of the fracture surface. XRD analysis of the deformed H2 specimen did not show XRD peaks associated with strain-induced martensite. A high SFE (49 $mJ \cdot m^{-2}$ for H2) promoted a dislocation glide-dominant deformation mechanism, which contributed to high hydrogen embrittlement resistance.

The designed V-microalloyed high Mn steel in the as-hot rolled condition exhibited degradation in notch tensile strength in a hydrogen charged environment (0.05 M NaOH - current density 1.65 $mA \cdot cm^{-2}$). Transgranular and intergranular brittle features were present at the notch root of the fracture surface of circumferentially notched tensile samples. The XRD result of the deformed V-microalloyed high Mn steel specimen indicated relatively low austenitic stability. However, the SFE for the designed V-microalloyed high Mn steel (47.3 $mJ \cdot m^{-2}$) is not

in the regime expected for deformation induced martensitic transformation. Notably, the SFE for the designed steel is only slightly lower compared to the H2 alloy (47.3 $mJ \cdot m^{-2}$ versus 49 $mJ \cdot m^{-2}$), but the hydrogen embrittlement sensitivity was significantly different between these two steels. These results imply that the SFE is not the only parameter that affects the hydrogen embrittlement resistance.

The 20-pct. cold worked only condition of the V-microalloyed high Mn steel has higher tensile strength properties and lower total elongation compared to 316L SS. The 20-pct. cold worked condition of V-microalloyed high Mn steel showed a slight degradation of notch tensile strength in a hydrogen charged environment (0.05 M NaOH - current density 1.65 $mA \cdot cm^{-2}$). Brittle features were present at the notch root of the fracture surface, implying hydrogen embrittlement.

The 20-pct. cold worked with aging (650 °C - 1h) condition of the V-microalloyed high Mn steel has higher ultimate tensile strength and comparable total elongation as compared to the as-received 316L SS. This condition of the V-microalloyed high Mn steel did not show strength degradation in a hydrogen charged environment (0.05 M NaOH - current density 1.65 $mA \cdot cm^{-2}$), indicating improvement of hydrogen embrittlement resistance after the post processing. The notch tensile strength of post processed condition was closer to that of 316L SS in hydrogen charged environment. Ductile features were present at the notch root of the fracture surface, thereby confirming the high hydrogen embrittlement resistance for the post processed condition.

Overall, the as-received H2 alloy and the 20-pct. cold worked with aging condition of V-microalloyed high Mn steel demonstrated high hydrogen embrittlement resistance. Further analysis should explore the mechanisms associated with the improved hydrogen embrittlement resistance, particularly in the cold worked and aged condition.

REFERENCES

1. S.K Dwivedi, and M. Vishwakarma, “Hydrogen embrittlement in different materials: A review,” *International Journal of Hydrogen Energy*, vol. 43, pp. 21603-21616, 2018.
2. O. Barrera, Bombac, Y. Chen, T.D. Daff, E. Galindo-Nava, P. Gong, and F. Sweeney, “Understanding and mitigating hydrogen embrittlement of steels: a review of experimental, modelling and design progress from atomistic to continuum,” *Journal of materials science*, vol. 53(9), pp. 6251-6290, 2018.
3. S.H Zaferani , R. Miresmaeiliand M.K Pourcharmi, “Mechanistic models for environmentally-assisted cracking in sour service,” *Engineering Failure Analysis*, 79, 672-703, 2017.
4. S. Wang, M.L Martin, I.M Robertson, and P. Sofronis, “Effect of hydrogen environment on the separation of Fe grain boundaries,” *Acta Materialia*, vol. 107, pp. 279-288, 2016.
5. M. S. Daw, and M.I Baskes, “Semiempirical, quantum mechanical calculation of hydrogen embrittlement in metals,” *Physical review letters*, vol. 50, pp. 1285, 1983.
6. K. N. Solanki, M.A Tschopp, M.A Bhatia, and N.R Rhodes, “Atomistic investigation of the role of grain boundary structure on hydrogen segregation and embrittlement in α-Fe,” *Metallurgical and Materials Transactions A*, vol. 44, pp. 1365-1375, 2013.
7. S. Plimpton, “Fast parallel algorithms for short-range molecular dynamics,” *Journal of computational physics*, vol. 117, pp. 1-19, 1995.
8. I.M Robertson, P. Sofronis, A. Nagao, M.L Martin, S. Wang, D.W Gross, and K.E Nygren, “Hydrogen embrittlement understood,” *Metallurgical and Materials Transactions A*, vol. 46, pp. 2323-2341, 2015.
9. C. D Beachem, “A new model for hydrogen-assisted cracking (hydrogen “embrittlement”),” *Metallurgical and Materials Transactions B*, vol. 3, pp. 441-455, 1972.
10. H.K. Birnbaum, R.P. Gangloff, M.B. Ives NACE, Houston, TX H.K. Birnbaum, in: "Environment Induced Cracking of Metals", Eds., R.P. Gangloff and M.B. Ives, NACE, Houston, TX, 1990, pp. 21-29.
11. H.K. Birnbaum, I.M. Robertson, P. Sofronis, and D. Teter, “Mechanisms of hydrogen related fracture--a review,” In Second International Conference on Corrosion-Deformation Interactions. CDI'96, pp. 172-195, 1996.
12. P.J Ferreira, I.M Robertson, H.K Birnbaum, “Hydrogen effects on the interaction between dislocations,” *Acta Mater*, vol. 46, pp.1749–1757, 1998.
13. Y. Nishino, M. Obata, and S. Asano, “Hydrogen-induced phase transformations in Fe50Ni50− xMnx alloys,” *Scripta Metallurgica et Materialia*, vol. 24, pp. 703-708, 1990.
14. N. Narita, and H.K Birnbaum, “On the role of phase transitions in the hydrogen embrittlement of stainless steels,” *Scripta Metallurgica*, vol. 14, pp. 1355-1358, 1980.

15. M. Martin, S. Weber, C. Izawa, S. Wagner, A. Pundt, and W. Theisen, “Influence of machining-induced martensite on hydrogen-assisted fracture of AISI type 304 austenitic stainless steel,” *International Journal of Hydrogen Energy*, vol. 36, pp. 11195-11206, 2011.

16. H.K.D.H Bhadeshia, “Prevention of hydrogen embrittlement in steels,” *ISIJ international*, vol. 56, pp. 24-36, 2016.

17. L.S Darken, and R.P Smith, “Behavior of hydrogen in steel during and after immersion in acid,” *Corrosion*, vol. 5, pp. 1-16, 1949.

18. I. Maroef, D. L. Olson, M. Eberhart and G. R. Edwards, “Hydrogen trapping in ferritic steel weld metal,” *International Materials Reviews*, vol. 47, pp. 191-223, 2002.

19. R. Silverstein, and D. Eliezer, “Mechanisms of hydrogen trapping in austenitic, duplex, and super martensitic stainless steels,” *Journal of Alloys and Compounds*, vol. 720, pp. 451-459, 2017.

20. A. McNabb, and P. K. Foster, “A new analysis of diffusion of hydrogen in iron and ferritic steels,” *Transactions of the Metallurgical Society of AIME*, vol. 227, pp. 618, 1963.

21. J.P Hirth, “Effects of hydrogen on the properties of iron and steel,” *Metallurgical Transactions A*, vol. 11, pp.861-890, 1980.

22. W.Y Choo, and J.Y Lee, “Thermal analysis of trapped hydrogen in pure iron,” *Metallurgical Transactions A*, vol. 13(1), pp. 135-140, 1982.

23. A.J Kumnick, and H.H Johnson, “Deep trapping states for hydrogen in deformed iron,” *Acta Metallurgica*, vol. 28, pp. 33-39, 1980.

24. I.M Bernstein, “The Effect of Hydrogen on the Deformation of Iron. CARNEGIE-MELLON UNIV PITTSBURGH PA METALS RESEARCH LAB, Feb 1, 1974.

25. K. Ono, and M. Meshii, “Hydrogen detrapping from grain boundaries and dislocations in high purity iron,” *Acta metallurgica et materialia*, vol. 40, pp.1357-1364, 1992.

26. T. Asaoka, C. Dagbert, M. Aucouturier, and J. Galland, “Quantitative Study of Trapping Characteristics of H in a Fe-0. 15 per Cent Ti Ferrite by High-Resolution Autoradiography and During Degassing at High Temperatures,” *Scr. Metall.*, vol. 11, pp.467-472, 1977.

27. J. L. Lee, and J.Y Lee, “Hydrogen trapping in AISI 4340 steel,” *Metal Science*, vol. 17, pp. 426-432, 1983.

28. K.Takai, Y.Homma, K. Izutsu, and M. Nagumo, “Identification of trapping sites in high-strength steels by secondary ion mass spectrometry for thermally desorbed hydrogen,” *Nippon Kinzoku Gakkaishi/Journal of the Japan Institute of Metals*, vol. 60, pp. 1155-1162, 1996.

29. E. Serra, A. Perujo, and G. Benamati, “Influence of traps on the deuterium behaviour in the low activation martensitic steels F82H and Batman,” *Journal of Nuclear Materials*, vol. 245, pp. 108-114, 1997.

30. A. I. Shirley, and C.K Hall, “Trapping of hydrogen by substitutional and interstitial impurities in α-iron. *Scripta metallurgica*,” vol. 17, pp. 1003-1008, 1983.

31. A. Turnbull, and R. B. Hutchings, “Analysis of hydrogen atom transport in a two-phase alloy,” *Materials Science and Engineering: A*, vol. 177, pp.161-171, 1994.

32. H. Asahi, D. Hirakami, and S. Yamasaki, “Hydrogen trapping behavior in vanadium-added steel,” *ISIJ international*, vol. 43, pp. 527-533, 2003.

33. B. Malard, B. Remy, C. Scott, A. Deschamps, J. Chêne, T. Dieudonné, and M.H Mathon, “Hydrogen trapping by VC precipitates and structural defects in a high strength Fe–Mn–C steel studied by small-angle neutron scattering,” *Materials Science and Engineering: A*, vol. 536, pp. 110-116, 2012.

34. F. Dong, J. Venezuela, H. Li, Z. Shi, Q. Zhou, L. Chen, J. Chen, L. Du, and A. Atrens. “Effect of vanadium and rare earth microalloying on the hydrogen embrittlement susceptibility of a Fe-18Mn-0.6 C TWIP steel studied using the linearly increasing stress test,” *Corrosion Science*, vol. 185, 2021.

35. Lin Zhang, Mao Wen, Masaaki Imade, Seiji Fukuyama, Kiyoshi Yokogawa, Effect of nickel equivalent on hydrogen gas embrittlement of austenitic stainless steels based on type 316 at low temperatures, Acta Materialia, Volume 56, Issue 14, 2008, Pages 3414-3421, ISSN 1359-6454, https://doi.org/10.1016/j.actamat.2008.03.022

36. G. Han, J. He, S. Fukuyama, and K. Yokogawa, “Effect of strain-induced martensite on hydrogen environment embrittlement of sensitized austenitic stainless steels at low temperatures,” *Acta materialia*, vol. 46, pp. 4559-4570, 1998.

37. T. Michler, C.S Marchi, J. Naumann, S. Weber, and M. Martin. "Hydrogen environment embrittlement of stable austenitic steels,” *International journal of hydrogen energy*, vol. 37, pp. 16231-16246, 2012.

38. Y.H Nam, J.S Park, U.B Baek, J.Y Suh, and S.H Nahm, “Low-temperature tensile and impact properties of hydrogen-charged high-manganese steel,” *International Journal of Hydrogen Energy*, vol. 44, pp. 7000-7013, 2019.

39. Yumi Ha, "Effect of Strain Rate on Deformation Behavior of Austenitic High Mn Steel at Cryogenic Temperature", Ph.D. Thesis, Pohang University of Science and Technology, Pohang, Korea, 2015.

40. D. Hull, and D.J Bacon, Introduction to dislocations, Elsevier vol. 37, 2011.

41. S. Weber, M. Martin, and W. Theisen, “Development of lean alloyed austeniticstainless steels with reduced tendency to hydrogen environment embrittlement,” Materials Science Forum. Vol. 706. Trans Tech Publications Ltd, 2012.

42. A. Dumay, J.P Chateau, S. Allain, S. Migot and O. Bouaziz, “Influence of addition elements on the stacking-fault energy and mechanical properties of an austenitic Fe–Mn–C steel,” *Materials Science and Engineering: A*, vol. 483, pp.184-187, 2008.

43. A. Saeed-Akbari, J. Imlau, U. Prahl, and W. Bleck, “Derivation and variation in composition-dependent stacking fault energy maps based on subregular solution model in high-manganese steels,” *Metallurgical and Materials Transactions A*, vol. 40, pp. 3076-3090, 2009.

44. S. Curtze, V.T Kuokkala, A. Oikari, J. Talonen and H. Hänninen, "Thermodynamic modeling of the stacking fault energy of austenitic steels," *Acta Materialia*, vol. 59, pp.1068-1076, 2011.

45. M. Koyama, S. Okazaki, T. Sawaguchi, and K. Tsuzaki, "Hydrogen embrittlement susceptibility of Fe-Mn binary alloys with high Mn content: effects of stable and metastable ε-martensite, and Mn concentration," *Metallurgical and Materials Transactions A*, 47(6), 2656-2673, 2016.

46. M. Koyama, H. Springer, S.V Merzlikin, K. Tsuzaki, E. Akiyama, and D. Raabe, "Hydrogen embrittlement associated with strain localization in a precipitation-hardened Fe–Mn–Al–C light weight austenitic steel," *International Journal of Hydrogen Energy*, vol. 39, pp. 4634-4646, 2014.

47. D.R Steinmetz, T. Jäpel, B. Wietbrock, P. Eisenlohr, I. Gutierrez-Urrutia, A. Saeed–Akbari, T. Hickel, F. Roters and D. Raabe, "Revealing the strain-hardening behavior of twinning-induced plasticity steels: Theory, simulations, experiments," *Acta Materialia*, vol. 61, pp. 494-510, 2013.

48. P.H Adler, G.B Olson and W.S Owen, "Strain hardening of Hadfield manganese steel," *Metallurgical and Materials Transactions A*, vol. 17, pp.1725-1737, 1986.

49. G.B. Olson, and M. Cohen, "A general mechanism of martensitic nucleation: Part II. FCC→ BCC and other martensitic transformations," *Metallurgical transactions A*, vol. 7, pp. 1905-1914, 1976.

50. S. Allain, J.P Chateau, O. Bouaziz, S. Migot, and N. Guelton, "Correlations between the calculated stacking fault energy and the plasticity mechanisms in Fe–Mn–C alloys," *Materials Science and Engineering: A*, vol. 387, pp. 158-162, 2004.

51. S.S Babu, E.D Specht, S.A David, E. Karapetrova, P. Zschack, M. Peet, and H.K.D.H Bhadeshia, "In-situ observations of lattice parameter fluctuations in austenite and transformation to bainite," *Metallurgical and Materials Transactions A*, vol. 36, pp. 3281-3289, 2005.

52. P.J Gibbs, P.D Hough, K. Thürmer, B.P Somerday, C. SanMarchi, and J.A Zimmerman, "Stacking fault energy-based alloy screening for hydrogen compatibility," *JOM*, vol. 72, pp. 1982-1992, 2020.

53. K. Ishida, "Direct estimation of stacking fault energy by thermodynamic analysis," *physica status solidi (a)*, vol. 36, pp. 717-728, 1976.

54. S.Takaki, H. Nakatsu, and Y.Tokunaga, "Effects of austenite grain size on ε martensitic transformation in Fe-15mass% Mn alloy," *Materials Transactions, JIM*, vol. 34, pp.489-495, 1993.

55. J.H. Jun, and C.S. Choi, "Variation of stacking fault energy with austenite grain size and its effect on the MS temperature of γ→ ε martensitic transformation in Fe–Mn alloy," *Materials Science and Engineering: A*, vol. 257, pp. 353-356, 1998.

56. A.T Dinsdale, "SGTE data for pure elements," *Calphad*, vol. 15, pp. 317-425, 1991.

57. S.T Pisarik, and D.C Van Aken, “Thermodynamic driving force of the γ→ ε transformation and resulting MS temperature in high-Mn steels,” *Metallurgical and Materials Transactions A,* vol. 47, pp.1009-1018, 2016.

58. Y.K Lee, and C. Choi, “Driving force for γ→ ε martensitic transformation and stacking fault energy of γ in Fe-Mn binary system,” *Metallurgical and Materials Transactions A,* vol. 31, pp.355-360, 2000.

59. J.F Breedis, and L. Kaufman, “The formation of Hcp and Bcc phases in austenitic iron alloys,” *Metallurgical Transactions,* vol. 2, pp. 2359-2371, 1971.

60. G. Inden, “The role of magnetism in the calculation of phase diagrams,” *Physica B+ C,* vol.103, pp. 82-100, 1981.

61. M. Hillert, and M. Jarl, “A model for alloying in ferromagnetic metals.” *Calphad,* vol. 2, pp.227-238, 1978.

62. T.Y Hsu, and X. Zuyao, “Martensitic transformation in Fe-Mn-Si based alloys,” *Materials Science and Engineering: A,* vol. 273, pp. 494-497, 1999.

63. N.I Medvedeva, M. S. Park, D. C. Van Aken, and J. E. Medvedeva. "First-principles study of the Mn, Al and C distribution and their effect on the stacking fault energies in austenite." *arXiv preprint arXiv:1208.0310,* 2012.

64. J.E. Jin, and Y.K. Lee, “Effects of Al on microstructure and tensile properties of C-bearing high Mn TWIP steel,” *Acta Materialia,* vol. 60, pp.1680-1688, 2012.

65. A. Das, “Revisiting stacking fault energy of steels,” *Metallurgical and materials transactions A,* vol. 47, pp. 748-768, 2016.

66. L.E Murr, “Microstructural changes associated with yielding and plastic flow in fcc metals and alloys." *Res mechanica,* vol. 9, pp. 159-187, 1983.

67. S.W Lee, and H.C Lee, “The mechanical stability of austenite and cryogenic toughness of ferritic Fe-Mn-AI Alloys,” *Metallurgical and Materials Transactions A,* vol. 24, pp. 1333-1343, 1993.

68. P.J Ferreira, and P. Müllner, “A thermodynamic model for the stacking-fault energy,” *Acta Materialia,* vol. 46, pp. 4479-4484, 1998

69. H.M Otte, “The formation of stacking faults in austenite and its relation to martensite,” *Acta Metallurgica,* vol. 5, pp. 614-627, 1957.

70. NY.Petrov and I.A Yakubstov, “Thermodynamic calculation of stacking fault energy for multicomponent alloys with f.c.c lattice based on iron,” *The Physics of Metals and Metallography,* vol. 62, pp. 34-38, 1986

71. V. Prokoshkina, and L. Kaputkina, “Peculiarities of martensitic transformations and martensite structure in high nitrogen steels,” *Materials Science and Engineering: A,* vol. 481, pp. 762-765, 2008.

72. L. Bracke, J. Penning, and N. Akdut, “The influence of Cr and N additions on the mechanical properties of FeMnC steels,” *Metallurgical and Materials Transactions A,* vol. 38, pp. 520-528, 2007.

73. J.K Kim, S.J Lee, and B.C De Cooman, “Effect of Al on the stacking fault energy of Fe-18Mn-0.6C twinning-induced plasticity,” *Scripta Materialia,* vol. 65, pp. 363-366, 2011

74. R Silverstein, D Eliezer, B Glam, S Eliezer, D Moreno, “Evaluation of Hydrogen Trapping Mechanisms during Performance of Different Hydrogen Fugacity in a Lean Duplex Stainless Steel,” *Journal of Alloys and Compounds,* vol. 648, pp. 601-608, 2015.

75. P. Kathayat, K. O Findley, J. G Speer and L. Cho. “Microstructural Engineering to Achieve Low Cost, High-Performance Solutions for hydrogen Storage,” Colorado School of Mines, ASPPRC Research Report No. MT-SRC-021-005, Plate and Hot-Rolled Steels, Mar. 1, 2021

76. I. Yoo, J.M Lee, H.S Lim, J.Y Suh, J. Lee and H. Byoungchul, "Comparative Study of Hydrogen Embrittlement of Three Heat-resistant Cr-Mo Steels Subjected to Electrochemical and Gaseous Hydrogen Charging." *Metallurgical and Materials Transactions A,* vol. 51, pp. 2118–2125, 2020.

77. J. Venezuela, E. Gray, Q. Liu, Q. Zhou, C. Tapia-Bastidas, M. Zhang, and A. Atrens, "Equivalent Hydrogen Fugacity during Electrochemical Charging of Some Martensitic Advanced High-Strength Steels." *Corrosion Science,* vol.127, pp.45-58, 2017.

78. D.P. Escobar, C. Miñambres, L. Duprez, K. Verbeken, M. Verhaege, "Internal and Surface Damage of Multiphase Steels and Pure Iron after Electrochemical Hydrogen Charging." *Corrosion Science,* vol. 53, pp. 3166-76, 2011.

79. R. Ueji, N. Tsuchida, D. Terada, N. Tsuji, Y. Tanaka, A. Takemura, K. Kunishige, "Tensile Properties and Twinning Behavior of High Manganese Austenitic Steel with Fine-Grained Structure." *Scripta Materialia*, vol. pp. 963-966, 2008.

80. O. Bouaziz, H. Zurob, B. Chehab, J. D. Embury, S. Allain and M. Huang, "Effect of Chemical Composition on Work Hardening of Fe—Mn—C TWIP Steels," *Materials Science and Technology*, vol. 27, pp. 707-709, 2011.

81. M. Huang, O. Bouaziz, D. Barbier and S. Allain, "Modelling the Effect of Carbon on Deformation Behaviour of Twinning Induced Plasticity Steels," *Journal of Material Science*, vol. 46, pp. 7410–7414, 2011

82. O. Bouaziz, S. Allain, C.P Scott, P. Cugy, D. Barbier, "High Manganese Austenitic Twinning Induced Plasticity Steels: A Review of the Microstructure Properties Relationships." *Current opinion in solid state and materials science,* vol. 15, pp. 141-68, 2011

83. J.B. Cohen and M. E. Fine, "Some Aspects of Short-Range Ordering," *Journal Physics Radium,* vol. 23 pp. 749-762, 1962.

84. H Kang, T. Ingendahl, J. Appen, R. Dronskowski, W. Bleck, "Impact of Short-Range Ordering on Yield Strength of High Manganese Austenitic Steels." *Materials Science and Engineering: A,* vol. 614, pp. 122-8, 2014.

85. J.D Yoo, K.T Park, "Microband-Induced Plasticity in a High Mn–Al–C light steel." *Materials Science and Engineering: A,* vol. 496, pp. 417-24, 2008

86. R. Scott, J.L Collet, A. Cael, C. Bao, F. Danoix, B. Malard, and C. Curfs, "Precipitation Strengthening in High Manganese Austenitic TWIP Steels." *International Journal of Materials Research*, vol. 102, pp. 538–549, 2011

87. M. Park, M.S Kang, G.W Park, E.Y Choi, H.C Kim, H.S Moon, J.B Jeon, H. Kim, S.H Kwon and B. Kim, "The effects of recrystallization on strength and impact toughness of cold-worked high-Mn austenitic steels." *Metals*, vol. 9, pp. 948, 2019.

88. S. Chen, R. Rana, A. Haldar, R.K Ray, "Current State of Fe-Mn-Al-C Low Density Steels." *Progress in Materials Science,* vol. 89, pp. 345-91, 2017.

89. R. Rana, C. Liu, R.K Ray, "Low-Density Low-Carbon Fe–Al Ferritic Steels." *Scripta Materialia* vol. 68, pp. 354-9, 2013.

90. C. San Marchi, B. P. Somerday, X. Tang, and G. H. Schiroky. "Effects of alloy composition and strain hardening on tensile fracture of hydrogen-precharged type 316 stainless steels*." International Journal of Hydrogen Energy,"* vol. 33, pp. 889-904, 2008.

91. B. Dutta, E.J Palmiere, C.M Sellars, "Modelling the Kinetics of Strain Induced Precipitation in Nb Microalloyed Steels." *Acta Materialia,* vol. 49, pp. 785-794, 2001.

92. B. Pereda, J.M RI, B. López, "Improved Model of Kinetics of Strain Induced Precipitation and Microstructure Evolution of Nb Microalloyed Steels during Multipass Rolling." *ISIJ international*, vol. 48, pp. 1457-1466, 2008.

93. Y. Zhou, Y. Liu, X. Zhou, C. Liu, J. Yu, Y. Huang, H. Li, and W. Li, "Precipitation and hot deformation behavior of austenitic heat-resistant steels: A review," *Journal of Materials Science & Technology,* vol. 33, pp.1448-1456, 2017.

94. E. Herms, J. M. Olive, and M. Puiggali, "Hydrogen embrittlement of 316L type stainless steel," *Materials Science and Engineering: A,* vol. 272, pp. 279-283, 1999.

95. I.B Tuğluca, M. Koyama, B. Bal, D. Canadinc, E. Akiyama, and K. Tsuzaki, "High-concentration carbon assists plasticity-driven hydrogen embrittlement in a Fe-high Mn steel with a relatively high stacking fault energy," *Materials Science and Engineering: A,* vol. 717, pp. 78-84, 2018.

96. M. Koyama, E. Akiyama, and K. Tsuzaki, "Hydrogen embrittlement in a Fe–Mn–C ternary twinning-induced plasticity steel," *Corrosion Science,* vol. 54, pp. 1-4, 2012.

97. R.E Reed-Hill, R. Abbaschian, Physical metallurgy principles (Vol. 17). New York: Van Nostrand.

98. Historical Data, London Metal Exchange (LME), 2021. available at https://www.lme.com/en/

99. S. Curtze, and V-T. Kuokkala, "Dependence of tensile deformation behavior of TWIP steels on stacking fault energy, temperature and strain rate," *Acta Materialia*, vol. 58, pp.5129-5141, 2010.

100. S Curtze, V-T. Kuokkala, A. Oikari, J. Talonen, and H. Hänninen, "Thermodynamic modeling of the stacking fault energy of austenitic steels," *Acta Materialia*, vol. 59, pp. 1068-1076, 2011.

101. A. Saeed-Akbari, J. Imlau, U. Prahl, and W. Bleck, “Derivation and variation in composition-dependent stacking fault energy maps based on subregular solution model in high-manganese steels,” *Metallurgical and Materials Transactions A*, vol. 40, pp. 3076-3090, 2009.

102. I.A Yakubtsov, A. Ariapour, and DD Perovic, “Effect of nitrogen on stacking fault energy of fcc iron-based alloys,” *Acta Materialia*, vol. 47(4), pp.1271-1279, 1999.

103. J. Kim, “Constitutive Modeling of the Tensile Behavior of TWIP Steels,” Ph.D. Thesis, Pohang University of Science and Technology, Pohang, Korea, 2012.

104. B. Kagay, "Hydrogen Embrittlement Assessment of Alloy 718 with Precipitate Variations," Ph.D. Thesis, Colorado School of Mines, Golden, CO, 2019.

105. Standard Test Methods for Determining Average Grain Size, ASTM E112.

106. Y. Kong, L. Cho, K.O. Findley, and J.G. Speer, “Microstructural Engineering of Mn-Alloyed Duplex Steels for Hydrogen Storage and Delivery,” Colorado School of Mines, ASPPRC Research Report No. MT-SRC-021-009, Sep. 2021.

107. C. San Marchi and B.P. Somerday, Sandia Report 2012-7321 - Technical Reference for Hydrogen Compatibility of Materials, Unlimited Release, Printed September 2012.

108. K. Yamada, M. Koyama, T. Kaneko, and K. Tsuzaki, “Positive and negative effects of hydrogen on tensile behavior in polycrystalline Fe–30Mn–(6− x) Si–xAl austenitic alloys,” *Scripta Materialia*, vol.105, pp. 54-57, 2015.

109. H.S. Noh, J.H. Kang, and S.J. Kim, “Effect of grain size on hydrogen embrittlement in stable austenitic high-Mn TWIP and high-N stainless steels,” *International Journal of Hydrogen Energy*, vol. 44, pp. 25076-25090, 2019.

110. N. Zan, H. Ding, X. Guo, Z. Tang, and W. Bleck, “Effects of grain size on hydrogen embrittlement in a Fe-22Mn-0.6 C TWIP steel,” *International Journal of Hydrogen Energy*, vol. 40(33), pp. 10687-10696, 2015.

111. BC De Cooman, Y. Estrin, and S.K Kim, “Twinning-induced plasticity (TWIP) Steels,” *Acta Materiala*, vol. 142, pp. 283-362, 2018.

112. J. Azevedo, A. Serrenho, and J. Allwood, “The deformation of metal powder particles: hardness and microstructure,” *Procedia Engineering*,” vol. 207, pp. 1200-1205, 2017.

113. L. Zhang, Z. Li, J. Zheng, Y. Zhao, P. Xu, C. Zhou, and X. Li, “Effect of strain-induced martensite on hydrogen embrittlement of austenitic stainless steels investigated by combined tension and hydrogen release methods,” *International journal of hydrogen energy*, vol. 38(19), pp. 8208-8214, 2013.

114. T. Michler, J. Naumann, M. Hock, K. Berreth, M.P Balogh, and E. Sattler, “Microstructural properties controlling hydrogen environment embrittlement of cold worked 316 type austenitic stainless steels,” *Materials Science and Engineering: A*, vol. 628, pp.252-261, 2015.

APPENDIX A: COPYRIGHT PERMISSIONS

SPRINGER NATURE LICENSE
TERMS AND CONDITIONS

Sep 27, 2022

This Agreement between Mr. Pawan Kathayat ("You") and Springer Nature ("Springer Nature") consists of your license details and the terms and conditions provided by Springer Nature and Copyright Clearance Center.

License Number	5397280748006	Will you be translating?	no
License date	Sep 27, 2022	Circulation/distribution	5000 - 9999
Licensed Content Publisher	Springer Nature	Author of this Springer Nature content	no
Licensed Content Publication	Metallurgical and Materials Transactions A	Title	Microstructural Engineering of Mn-Alloyed Austenitic Steel for Hydrogen Storage and Delivery
Licensed Content Title	Hydrogen Embrittlement Understood	Institution name	Colorado School of Mines
Licensed Content Author	Ian M. Robertson et al	Expected presentation date	Sep 2022
Licensed Content Date	Mar 28, 2015	Portions	Figure 1
Type of Use	Thesis/Dissertation	Requestor Location	Mr. Pawan Kathayat 3130 Indiana Street GOLDEN, CO 80401 United States Attn: Mr. Pawan Kathayat
Requestor type	academic/university or research institute		
Format	print and electronic		
Portion	figures/tables/illustrations		
Number of figures/tables /illustrations	1		

Figure A.1: Copyright permission for the Figure 2.1 in the background chapter.

ELSEVIER LICENSE
TERMS AND CONDITIONS

Oct 04, 2022

This Agreement between Mr. Pawan Kathayat ("You") and Elsevier ("Elsevier") consists of your license details and the terms and conditions provided by Elsevier and Copyright Clearance Center.

License Number	5402170232710
License date	Oct 04, 2022
Licensed Content Publisher	Elsevier
Licensed Content Publication	Materials Science and Engineering: A
Licensed Content Title	Hydrogen embrittlement of 316L type stainless steel
Licensed Content Author	E Herms,J.M Olive,M Puiggali
Licensed Content Date	Nov 30, 1999
Licensed Content Volume	272
Licensed Content Issue	2
Licensed Content Pages	5
Start Page	279
End Page	283

Type of Use	reuse in a thesis/dissertation
Portion	figures/tables/illustrations
Number of figures/tables /illustrations	1
Format	both print and electronic
Are you the author of this Elsevier article?	No
Will you be translating?	No
Title	Microstructural Engineering of Mn-Alloyed Austenitic Steel for Hydrogen Storage and Delivery
Institution name	Colorado School of Mines
Expected presentation date	Oct 2022
Portions	Figure 2
Requestor Location	Mr. Pawan Kathayat 3130 Indiana Street GOLDEN, CO 80401 United States Attn: Mr. Pawan Kathayat

Figure A.2: Copyright permission for the Figure 2.3 in the background chapter.

ELSEVIER LICENSE
TERMS AND CONDITIONS

Oct 04, 2022

This Agreement between Mr. Pawan Kathayat ("You") and Elsevier ("Elsevier") consists o your license details and the terms and conditions provided by Elsevier and Copyright Clearance Center.

License Number	5402170532468
License date	Oct 04, 2022
Licensed Content Publisher	Elsevier
Licensed Content Publication	Corrosion Science
Licensed Content Title	Hydrogen embrittlement in a Fe–Mn–C ternary twinning-induced plasticity steel
Licensed Content Author	Motomichi Koyama,Eiji Akiyama,Kaneaki Tsuzaki
Licensed Content Date	Jan 1, 2012
Licensed Content Volume	54
Licensed Content Issue	n/a
Licensed Content Pages	4
Start Page	1
End Page	4

Type of Use	reuse in a thesis/dissertation
Portion	figures/tables/illustrations
Number of figures/tables /illustrations	1
Format	both print and electronic
Are you the author of this Elsevier article?	No
Will you be translating?	No
Title	Microstructural Engineering of Mn-Alloyed Austenitic Steel for Hydrogen Storage and Delivery
Institution name	Colorado School of Mines
Expected presentation date	Oct 2022
Portions	Fig 5
Requestor Location	Mr. Pawan Kathayat 3130 Indiana Street GOLDEN, CO 80401 United States Attn: Mr. Pawan Kathayat

Figure A.3: Copyright permission for the Figure 2.4 in the background chapter.

SPRINGER NATURE LICENSE
TERMS AND CONDITIONS

Oct 04, 2022

This Agreement between Mr. Pawan Kathayat ("You") and Springer Nature ("Springer Nature") consists of your license details and the terms and conditions provided by Springer Nature and Copyright Clearance Center.

License Number	5402171356902
License date	Oct 04, 2022
Licensed Content Publisher	Springer Nature
Licensed Content Publication	JOM Journal of the Minerals, Metals and Materials Society
Licensed Content Title	Stacking Fault Energy Based Alloy Screening for Hydrogen Compatibility
Licensed Content Author	P. J. Gibbs et al
Licensed Content Date	Mar 30, 2020
Type of Use	Thesis/Dissertation
Requestor type	academic/university or research institute
Format	print and electronic
Portion	figures/tables/illustrations
Number of figures/tables /illustrations	1

Will you be translating?	no
Circulation/distribution	5000 - 9999
Author of this Springer Nature content	no
Title	Microstructural Engineering of Mn-Alloyed Austenitic Steel for Hydrogen Storage and Delivery
Institution name	Colorado School of Mines
Expected presentation date	Oct 2022
Portions	Figure 2
Requestor Location	Mr. Pawan Kathayat 3130 Indiana Street GOLDEN, CO 80401 United States Attn: Mr. Pawan Kathayat

Figure A.4: Copyright permission for the Figure 2.7 in the background chapter.

SPRINGER NATURE LICENSE
TERMS AND CONDITIONS

Oct 04, 2022

This Agreement between Mr. Pawan Kathayat ("You") and Springer Nature ("Springer Nature") consists of your license details and the terms and conditions provided by Springer Nature and Copyright Clearance Center.

License Number	5402180283704	Will you be translating?	no
License date	Oct 04, 2022	Circulation/distribution	1000 - 1999
Licensed Content Publisher	Springer Nature	Author of this Springer Nature content	no
Licensed Content Publication	Metallurgical and Materials Transactions A	Title	Microstructural Engineering of Mn-Alloyed Austenitic Steel for Hydrogen Storage and Delivery
Licensed Content Title	Revisiting Stacking Fault Energy of Steels	Institution name	Colorado School of Mines
Licensed Content Author	Arpan Das	Expected presentation date	Oct 2022
Licensed Content Date	Dec 14, 2015	Portions	Figure 15 (a), (c), (d), (e)
Type of Use	Thesis/Dissertation	Requestor Location	Mr. Pawan Kathayat 3130 Indiana Street GOLDEN, CO 80401 United States Attn: Mr. Pawan Kathayat
Requestor type	academic/university or research institute		
Format	print and electronic		
Portion	figures/tables/illustrations		
Number of figures/tables /illustrations	4		

Figure A.5: Copyright permission for the Figure 2.8 in the background chapter.

ELSEVIER LICENSE
TERMS AND CONDITIONS

Oct 04, 2022

This Agreement between Mr. Pawan Kathayat ("You") and Elsevier ("Elsevier") consists of your license details and the terms and conditions provided by Elsevier and Copyright Clearance Center.

License Number	5402181367112
License date	Oct 04, 2022
Licensed Content Publisher	Elsevier
Licensed Content Publication	Scripta Materialia
Licensed Content Title	Tensile properties and twinning behavior of high manganese austenitic steel with fine-grained structure
Licensed Content Author	R. Ueji,N. Tsuchida,D. Terada,N. Tsuji,Y. Tanaka Takemura,K. Kunishige
Licensed Content Date	Nov 1, 2008
Licensed Content Volume	59
Licensed Content Issue	9
Licensed Content Pages	4
Start Page	963
End Page	966

Type of Use	reuse in a thesis/dissertation
Portion	figures/tables/illustrations
Number of figures/tables /illustrations	1
Format	both print and electronic
Are you the author of this Elsevier article?	No
Will you be translating?	No
Title	Microstructural Engineering of Mn-Alloyed Austenitic Steel for Hydrogen Storage and Delivery
Institution name	Colorado School of Mines
Expected presentation date	Oct 2022
Portions	Figure 2
	Mr. Pawan Kathayat 3130 Indiana Street

Figure A.6: Copyright permission for the Figure 2.11 in the background chapter.

ELSEVIER LICENSE
TERMS AND CONDITIONS

Oct 04, 2022

This Agreement between Mr. Pawan Kathayat ("You") and Elsevier ("Elsevier") consists of your license details and the terms and conditions provided by Elsevier and Copyright Clearance Center.

License Number	5402200178749
License date	Oct 04, 2022
Licensed Content Publisher	Elsevier
Licensed Content Publication	International Journal of Hydrogen Energy
Licensed Content Title	Effects of alloy composition and strain hardening on tensil fracture of hydrogen-precharged type 316 stainless steels
Licensed Content Author	C. San Marchi,B.P. Somerday,X. Tang,G.H. Schiroky
Licensed Content Date	Jan 1, 2008
Licensed Content Volume	33
Licensed Content Issue	2
Licensed Content Pages	16
Start Page	889
End Page	904

Type of Use	reuse in a thesis/dissertation
Portion	figures/tables/illustrations
Number of figures/tables /illustrations	2
Format	both print and electronic
Are you the author of this Elsevier article?	No
Will you be translating?	No
Title	Microstructural Engineering of Mn-Alloyed Austenitic Steel for Hydrogen Storage and Delivery
Institution name	Colorado School of Mines
Expected presentation date	Oct 2022
Portions	Figure 2(a) and (b)
Requestor Location	Mr. Pawan Kathayat 3130 Indiana Street GOLDEN, CO 80401 United States Attn: Mr. Pawan Kathayat

Figure A.7: Copyright permission for the Figure 2.14 in the background chapter.

ELSEVIER LICENSE
TERMS AND CONDITIONS

Oct 04, 2022

This Agreement between Mr. Pawan Kathayat ("You") and Elsevier ("Elsevier") consists of your license details and the terms and conditions provided by Elsevier and Copyright Clearance Center.

License Number	5402200587415	End Page	608
License date	Oct 04, 2022	Type of Use	reuse in a thesis/dissertation
		Portion	figures/tables/illustrations
Licensed Content Publisher	Elsevier	Number of figures/tables /illustrations	1
Licensed Content Publication	Journal of Alloys and Compounds	Format	both print and electronic
		Are you the author of this Elsevier article?	No
Licensed Content Title	Evaluation of hydrogen trapping mechanisms during performance of different hydrogen fugacity in a lean duplex stainless steel	Will you be translating?	No
		Title	Microstructural Engineering of Mn-Alloyed Austenitic Steel for Hydrogen Storage and Delivery
Licensed Content Author	R. Silverstein,D. Eliezer,B. Glam,S. Eliezer,D. Moreno	Institution name	Colorado School of Mines
		Expected presentation date	Oct 2022
Licensed Content Date	Nov 5, 2015	Portions	Figure 4
Licensed Content Volume	648	Requestor Location	Mr. Pawan Kathayat 3130 Indiana Street GOLDEN, CO 80401 United States Attn: Mr. Pawan Kathayat
Licensed Content Issue	n/a		
Licensed Content Pages	8		
Start Page	601		

Figure A.8: Copyright permission for the Figure 2.15 in the background chapter.